

# Pressure–temperature–structural distance relationships within Greater Himalayan rocks in eastern Bhutan: implications for emplacement models

K. S. AGUSTSSON,<sup>1</sup> S. M. GORDON,<sup>1</sup> S. P. LONG,<sup>2,\*</sup> G. G. E. SEWARD,<sup>3</sup> K. ZEIGER<sup>1</sup> AND M. PENFOLD<sup>1</sup>

<sup>1</sup>Department of Geological Sciences, University of Nevada, Reno, NV, USA (staciag@unr.edu)

<sup>2</sup>Nevada Bureau of Mines and Geology, University of Nevada, Reno, NV, USA

<sup>3</sup>Earth Research Institute, University of California, Santa Barbara, CA, USA

**ABSTRACT** In the Himalayan orogen, Greater Himalayan (GH) rocks were buried to mid- to lower-crustal levels and are now exposed across the strike of the orogen. Within the eastern Himalaya, in the Kingdom of Bhutan, the GH is divided into structurally lower (lower-GH) and upper (upper-GH) levels by the Kakhtang thrust (KT). Pressure–temperature estimates from lower- and upper-GH rocks collected on two transects across the KT yield similar  $P$ – $T$ –structural distance trends across each transect. In the eastern transect, temperatures are similar (from 730 to 650 °C) over a structural thickness of ~11 km, but peak pressures decrease from ~10 to 6 kbar with increasing structural level. In comparison, peak temperatures in the central Bhutan transect are similar (from 730 to 600 °C), but pressures decrease from 10 to 6.5 kbar with increasing structural level over a structural thickness of ~6 km. The structurally highest sample reveals slightly higher pressures of 8.0 kbar in comparison to pressures of ~6.5 kbar for samples collected from within the KT zone, ~4 km below. Within each transect, there are increases in pressure  $\pm$  temperature within the overall upright  $P$ – $T$  gradient that may demarcate intra-GH shear zone(s). These  $P$ – $T$  results combined with evidence that the timing of initial melt crystallization becomes older with increasing structural level suggest that the intra-GH shear zones emplaced deeper GH rocks via progressive ductile underplating. These shear zones, including the KT, likely aided in the initial emplacement and construction of the GH as a composite tectonic unit during the Late Oligocene to Early Miocene, from *c.* 27 to 16 Ma.

**Key words:** Bhutan; emplacement mechanisms; Greater Himalaya; thermobarometry; thinning.

## INTRODUCTION

Investigations of deeply exhumed rocks within active continent–continent collisional orogens provide insights into the dynamic links between processes that act at lower-, middle- and upper-crustal levels during orogenesis. These studies also provide a present-day analogue into the orogenic evolution and architecture of ancient collisional orogenic systems (e.g. Grenville; McLelland *et al.*, 2010).

The Himalayan–Tibetan orogen, the largest active orogenic system on Earth, is the result of the poly-phase closure of the Tethyan ocean basin, culminating in the collision of India and Asia at *c.* 55 Ma (e.g. Rowley, 1996; Leech *et al.*, 2005). The Himalayan orogenic belt makes up the southern part of this collisional system, and for ~2000 km along the strike of the orogen, a package of middle- to lower-crustal rocks, referred to here as the Greater Himalayan

(GH) rocks, is exposed (Fig. 1). The GH rocks were buried to upper-amphibolite, and locally granulite and/or eclogite facies conditions prior to their exhumation (e.g. Gansser, 1964; Hodges, 2000; Yin & Harrison, 2000). The GH rocks exposed throughout the Himalayan orogen represent an excellent unit and location to investigate the processes active at mid-crustal levels during active convergence.

The GH rocks are bounded by the top-to-the-south Main Central thrust (MCT) below and the top-to-the-north Southern Tibetan detachment (STD) system above (e.g. Gansser, 1964; LeFort, 1975; Burchfiel *et al.*, 1992; Hodges, 2000; Fig. 1). In the eastern Himalaya within the Kingdom of Bhutan, a top-to-the-south sense shear zone, named the Kakhtang thrust (KT) in central/eastern Bhutan and the Laya thrust in western Bhutan, has been proposed to divide the GH into structurally upper (upper-GH) and structurally lower (lower-GH) levels (Swapp & Hollister, 1991; Grujic *et al.*, 1996, 2002, 2011; Davidson *et al.*, 1997; Hollister & Grujic, 2006; Warren *et al.*, 2011, 2014; Fig. 1).

\*Present address: School of the Environment, Washington State University, Pullman, WA, USA.

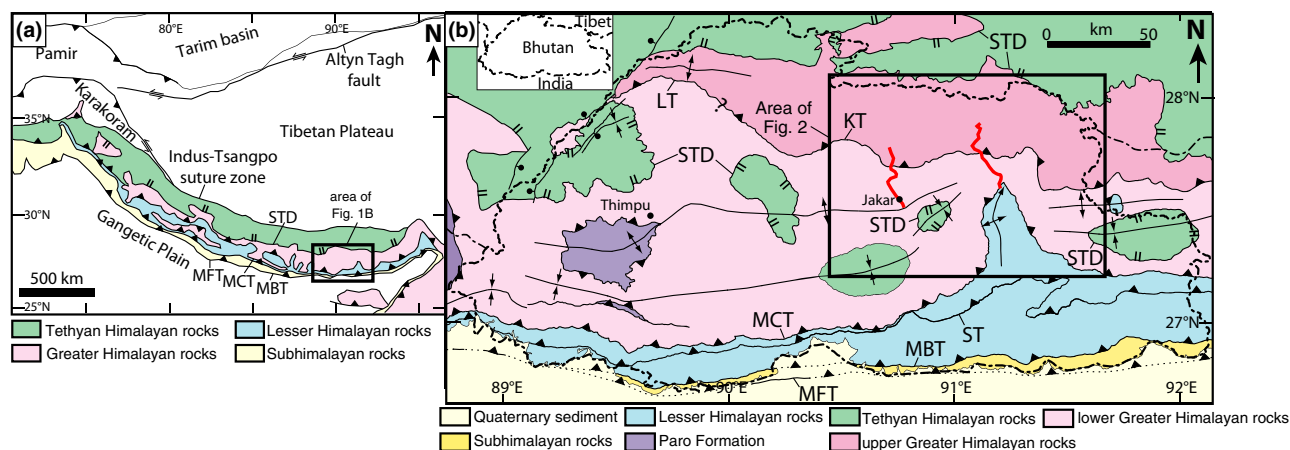


**Fig. 1.** (a) Simplified geological map of the Himalayan orogeny showing the four main tectonostratigraphic zones exposed across the strike of the orogen (simplified from Yin, 2006). (b) Simplified geological map of Bhutan modified from Long *et al.* (2011a). Box marks the area shown in Fig. 2. Mapping and sampling transects are highlighted in red. MFT, Main Frontal thrust; MBT, Main Boundary thrust; MCT, Main Central thrust; STD, South Tibetan Detachment system; KT, Kakhtang thrust; LT, Laya thrust.

Multiple petrological investigations in Bhutan have focused on characterizing the  $P$ – $T$  conditions of GH rocks, specifically in proximity to first-order structures including the MCT and Laya thrust (e.g. Swapp & Hollister, 1991; Grujic *et al.*, 1996; Davidson *et al.*, 1997; Daniel *et al.*, 2003; Long *et al.*, 2011c; Warren *et al.*, 2011, 2012; Corrie *et al.*, 2012); however, most of these studies have focused on either the upper-GH rocks in western Bhutan or lower-GH rocks. To date, no published quantitative  $P$ – $T$  data exist for upper-GH rocks in central and eastern Bhutan, despite their potential to preserve evidence for the conditions of metamorphism that can be used, along with geochronological and structural data, to understand their burial and exhumation history.

This study presents detailed petrology and  $P$ – $T$  data for metapelites and gneisses collected in two transects that cross the KT in north-central and northeastern Bhutan, including samples from both the lower- and upper-GH (Fig. 2). The peak and near-peak  $P$ – $T$  conditions are used to document pressure and temperature gradients across the sampled structural thickness of the GH to understand the post-burial history of the GH in central and eastern Bhutan. In addition, this petrological study is used to evaluate GH rocks in Bhutan in the context of several models for Himalayan tectonics, including construction of the GH rocks as a composite unit through progressive ductile underplating (e.g. Carosi *et al.*, 2010; Larson & Cottle, 2014).

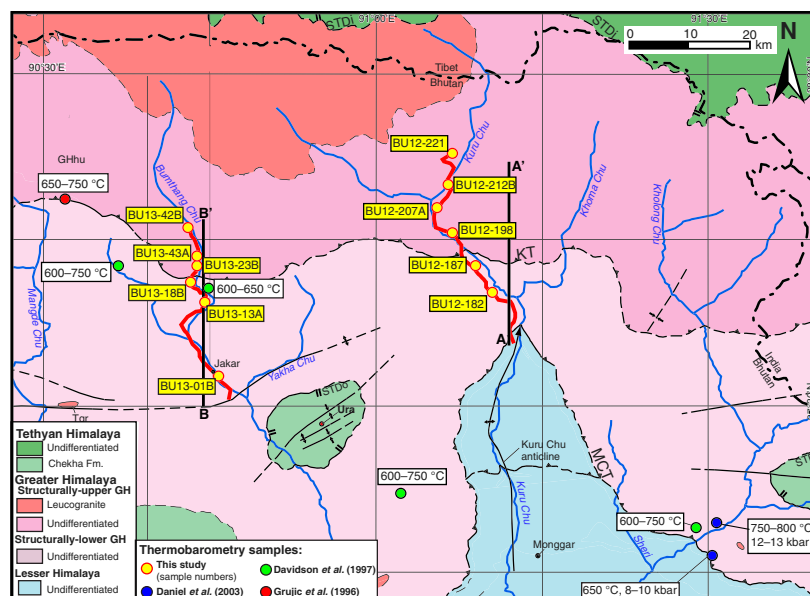
## GEOLOGICAL BACKGROUND

### Geological framework

The Himalayan orogenic belt has been subdivided into four simplified tectonostratigraphic zones,

including the sub-Himalaya, Lesser Himalaya, Greater Himalaya and Tethyan Himalaya, which are oriented parallel to the strike of the orogen and separated by major brittle and ductile fault zones (e.g. Gansser, 1964; LeFort, 1975; Yin, 2006; Fig. 1a). On the southern margin of the Himalayan orogenic belt, the sub-Himalaya consists of Neogene–Quaternary synorogenic rocks deposited in a flexural foreland basin. These rocks are structurally overlain by Lesser Himalayan rocks across the Main Boundary thrust (Heim & Gansser, 1939; Gansser, 1964). The Lesser Himalayan section consists of Palaeoproterozoic–Tertiary unmetamorphosed sedimentary rocks and greenschist facies metasedimentary rocks and orthogneiss (e.g. Myrow *et al.*, 2009; Kohn *et al.*, 2010; Long *et al.*, 2011d; Martin *et al.*, 2011). Greater Himalayan rocks are thrust above Lesser Himalayan rocks across the MCT, and they are predominantly upper-amphibolite facies metasedimentary rocks, orthogneiss and leucogranite sheets and plutons (e.g. Gansser, 1964; LeFort, 1975; Grujic *et al.*, 1996; Harrison *et al.*, 1997). The protoliths of both GH and Lesser Himalayan rocks are interpreted to be sedimentary rocks deposited on the northern margin of the Indian plate (LeFort, 1975; LeFort *et al.*, 1987; Burchfiel *et al.*, 1992; Hodges, 2000; Yin, 2006), although GH rocks have also been interpreted as allochthonous relative to India (DeCelles *et al.*, 2000). The GH rocks are mostly exposed between the top-to-the-south MCT (e.g. Gansser, 1964; LeFort, 1975) and the top-to-the-north STD system (e.g. Burchfiel *et al.*, 1992; Yin, 2006). Structurally above the STD, the Tethyan Himalaya consists of greenschist facies metasedimentary rocks and unmetamorphosed sedimentary rocks that were deposited on the southern passive margin of the Tethyan ocean basin that once separated India from Asia (e.g. Gaetani & Garzanti,

**Fig. 2.** Simplified geological map of eastern Bhutan modified from Long *et al.* (2011a). Mapping and sampling transects are highlighted in red. Published thermobarometry results are shown with white labels with points in green (Davidson *et al.*, 1997), blue (Daniel *et al.*, 2003) and red (Grujic *et al.*, 1996), and samples from this study are shown with a yellow label and point. A to A' and B to B' lines indicate the location of the cross-sections shown in Fig. S1. The undifferentiated unit in the Greater Himalaya and Lesser Himalaya rocks includes both metasedimentary and orthogneiss lithologies. GH, Greater Himalaya; LH, Lesser Himalaya; MCT, Main Central thrust; STDi, inner Southern Tibetan detachment; STDu, outer Southern Tibetan detachment; KT, Kakhtang thrust.



1991; Brookfield, 1993; Garzanti, 1999). To the north, the Tethyan Himalaya is bound by the Indus-Tsangpo suture zone, which marks the boundary between the Indian and Eurasian plates (e.g. Yin, 2006).

### Geological setting of Bhutan

In Bhutan, the GH consists of up to ~20 km (structural thickness) of orthogneiss, metasedimentary rocks and leucogranite (e.g. Gansser, 1983; Swapp & Hollister, 1991; Grujic *et al.*, 2002; Long *et al.*, 2011a; Figs 1b, 2 & S1). As described above, within the GH in Bhutan, a north-dipping, top-to-the-south ductile shear zone, named the KT in central and eastern Bhutan, and the Laya thrust in northwestern Bhutan, has been proposed to divide the GH rocks into structurally upper (upper-GH) and structurally lower (lower-GH) units (e.g. Swapp & Hollister, 1991; Grujic *et al.*, 1996, 2002, 2011; Warren *et al.*, 2011, 2012). The KT has been mapped, in part, by the apparent up-section crossing of the second-sillimanite isograd (muscovite-out reaction) boundary and by an increase in the volume percentage of leucocratic material within migmatites (e.g. Gansser, 1983; Swapp & Hollister, 1991; Grujic *et al.*, 1996, 2002). The KT is interpreted to be younger than the structurally underlying MCT, and therefore represents an out-of-sequence shear zone (Grujic *et al.*, 2002); U–Pb monazite and xenotime crystallization ages of *c.* 15–14 Ma from shear bands in-filled with leucocratic material have been interpreted to bracket the maximum age of motion on the KT in central Bhutan (Daniel *et al.*, 2003). In western Bhutan, the Laya thrust was likely active from *c.* 14–10 Ma (Grujic *et al.*, 2011; Warren *et al.*, 2011). The Zimithang thrust, which is interpreted as the along-strike equivalent of the KT to the east in Arunachal Pradesh,

was active from *c.* 15–12 Ma (Warren *et al.*, 2014). Below, we describe the previous data and interpretations from the lower- and upper-GH within the Bhutan Himalaya.

### Lower-GH

Previous studies of lower-GH rocks document *P*–*T* conditions consistent with upper-amphibolite facies metamorphism. In the MCT zone in easternmost Bhutan, kyanite-bearing migmatite and schist record peak temperatures of 600–750 °C at 8–10 kbar, which increase to 750–800 °C at 10–14 kbar for kyanite-bearing migmatite within the middle of the lower-GH unit (Davidson *et al.*, 1997; Daniel *et al.*, 2003; Fig. 2). In central Bhutan, previous studies document the opposite trend, with peak temperatures of 600–700 °C at 10–11 kbar at the base of the lower-GH, which decrease systematically with structural distance from the MCT to 550–600 °C and 7–9 kbar at the top of the unit (Corrie *et al.*, 2012). In addition, peak *P*–*T* estimates of 600–650 °C and 6–7 kbar for staurolite–kyanite–garnet metapelites have been reported in north-central Bhutan, in the immediate footwall of the KT (Swapp & Hollister, 1991; Davidson *et al.*, 1997). In western Bhutan, garnet amphibolite in the structurally lowest levels of the lower-GH records higher *P*–*T* conditions (~740 °C and 8 kbar; Warren *et al.*, 2012) in comparison to rocks at similar structural levels to the east. Rocks in the immediate footwall of the Laya thrust record lower temperatures (~650 °C), but higher pressures (>10 kbar) (Warren *et al.*, 2011).

Monazite from gneiss at structurally high levels of the lower-GH in western Bhutan records sillimanite-grade metamorphism at *c.* 21–15 Ma (Kellett *et al.*, 2010; Warren *et al.*, 2011). In contrast, in eastern

Bhutan, monazite from structurally lower kyanite-bearing schist is interpreted to date prograde metamorphism from *c.* 24–22 Ma followed by melt crystallization at *c.* 15–14 Ma (monazite and xenotime; Daniel *et al.*, 2003). Additional samples across the structural thickness of the lower-GH in central and eastern Bhutan document a protracted metamorphic history from *c.* 33–14 Ma, with melt crystallization from *c.* 15–14 Ma (Zeiger *et al.*, 2015).

The STD juxtaposes Tethyan Himalayan rocks above the GH throughout the Himalaya. Within central and southern Bhutan, greenschist facies to lower amphibolite facies rocks have been interpreted as klippen of Tethyan Himalayan rocks preserved above the STD (Grujic *et al.*, 2002; Kellett *et al.*, 2009; Long *et al.*, 2011a; Cooper *et al.*, 2013; Fig. 1b). Because of these apparent klippen, the STD is mapped as two distinct segments: a ductile–brittle shear zone located in northernmost Bhutan and southern Tibet that separates the upper-GH from Tethyan Himalayan rocks (inner-STD; e.g. Burchfiel *et al.*, 1992; Kellett *et al.*, 2009) (Figs 1b & 2), and a ductile structure located at the base of the klippen of Tethyan Himalayan rocks (outer-STD; e.g. Grujic *et al.*, 2002; Hollister & Grujic, 2006; Kellett *et al.*, 2009) (Figs 1b & 2). The location of the outer-STD in central Bhutan is debated (e.g. Long *et al.*, 2011a; Corrie *et al.*, 2012; Cooper *et al.*, 2013; Greenwood *et al.*, 2015).

Previous studies of the lower-GH interpreted that these amphibolite-facies rocks were emplaced via channelized flow (i.e. the channel-flow model of Beaumont *et al.*, 2001) between the MCT and the outer-STD (Grujic *et al.*, 1996, 2002). However, mapping and petrology in south-central Bhutan suggests that displacement along the outer-STD is minor (~10's of km as opposed to the 100's of km required for large-scale channel flow), that there is not a significant change in *P–T* conditions across the structural level that has previously been mapped as the outer-STD and that there is no evidence for melting in the structurally higher levels of the lower-GH (Long & McQuarrie, 2010; Corrie *et al.*, 2012). An alternate model, with top-to-the-south emplacement of a ductile thrust sheet consisting of lower-GH rocks, accompanied by layer-normal thinning and distributed north-vergent shear at high structural levels, has been proposed for south-central Bhutan (Long & McQuarrie, 2010; Corrie *et al.*, 2012).

#### Upper-GH

Structurally above the KT, the upper-GH records predominantly upper-amphibolite facies, or locally granulite to eclogite facies conditions, contains a high percentage (20–70 vol.%) of leucocratic material in many outcrops and exhibits regional-scale (~100's of km<sup>2</sup>) leucogranite bodies (Gansser, 1983; Swapp & Hollister, 1991; Davidson *et al.*, 1997). To date,

petrological and structural studies of the upper-GH have been focused in northwestern Bhutan. There, rare granulitized eclogites record eclogite facies metamorphism (~760 °C and >15 kbar) at *c.* 15 Ma followed by a granulite facies overprint (~800–850 °C and 9–11 kbar) at *c.* 14 Ma, implying rapid exhumation rates (2–4 cm yr<sup>-1</sup>; e.g. Grujic *et al.*, 2011; Warren *et al.*, 2012). Analysis of mafic and pelitic granulites that host the rare granulitized eclogites record peak temperatures of ~750–800 °C (Warren *et al.*, 2011).

In contrast to the abundant thermobarometric studies conducted in northwestern Bhutan, only a single deformation temperature of 650–750 °C (quartz prism (c)-slip; Grujic *et al.*, 1996) from a leucogranite dyke in the KT zone has been determined from the upper-GH in central and eastern Bhutan (Fig. 2). A U–Th–Pb monazite and zircon study documents metamorphism from *c.* 36–14 Ma with melt crystallization from *c.* 27–16 Ma for rocks within the upper-GH in north-central and northeastern Bhutan (Zeiger *et al.*, 2015). The initiation of melt crystallization within these rocks becomes progressively older with increasing structural position above the KT.

#### Geology of the GH in north-central and northeastern Bhutan

To understand the burial and exhumation history of GH rocks in north-central and northeastern Bhutan, field work was conducted and samples were collected along two across-strike transects that cross the KT, one in northeastern Bhutan (the Kuru Chu transect) and one in north-central Bhutan (the Bumthang Chu transect) (Table 1; Fig. 2). The transects cover a structural thickness of ~15 km and ~12 km, respectively (Fig. S1).

The two transects reveal lithological, structural and petrological similarities. Along the northeastern transect, directly above the MCT, the lower-GH consists of migmatitic, garnet-bearing schist and metapelite that are interlayered with siliceous gneiss and orthogneiss. About 4 km structurally above the MCT, the lower-GH transitions to massive quartzite interlayered with schist. Kellett *et al.* (2010) mapped this quartzite as part of the Tethyan Himalayan Chekha Group and interpreted the contact at its base as the outer-STD; however, based on our mapping and the mapping of Long *et al.* (2011a,b), we include these metasedimentary rocks as part of the lower-GH unit. We did not observe evidence for a north-vergent shear zone localized at their basal contact. Above the quartzite (~6 km structurally above the MCT), migmatitic gneiss, with leucosomes representing ~30 vol.% of the outcrops (Fig. 3a), is observed. The transition from quartzite to migmatite marks the previously mapped location of the KT in northeastern Bhutan (Grujic *et al.*, 1996, 2002).



**Table 1.** Major silicate mineral assemblages for the central and eastern Bhutan studied samples<sup>a</sup>.

	Rock type	Garnet (form) <sup>b</sup>	Ky	Sil <sup>c</sup>	St	Pl	Kfs <sup>d</sup>	Amp	Ms	Accessory phases
Structurally Upper Greater Himalaya (Upper-GH)										
BU12-221	Sillimanite-bearing orthogneiss	i, s		x		x	x		x	zrn
BU12-212B	Sillimanite–garnet metapelite	i, e		x		t	K		t	ilm, mnz, zrn
BU13-42B	Amphibolite–garnet orthogneiss	s, xg, e				x		x		ap, ilm, spn, zrn
BU12-207A	Sillimanite–garnet metapelite	i, e		x		x			x	ap, ilm, tur, zrn
BU13-43A	Sillimanite-bearing paragneiss	s		x		x				ap, ilm, tur, zrn
BU13-23B	Kyanite–sillimanite–garnet metapelite	i, e	x	x		x	t		x	ap, ilm, mnz, ru, tur, zrn
BU12-198	Sillimanite–garnet metapelite	i, e		x		x			x	ilm, mnz, zrn
Structurally Lower Greater Himalayan (Lower-GH)										
BU13-18B	Staurolite–garnet schist	i, s		x	x	x			x	ilm, tur
BU13-13A	Sillimanite-bearing siliceous gneiss	i, s		x	x	x			x	ilm, tur
BU12-187	Kyanite–garnet metapelite	i, s	x	t, r?		x	x		x	ilm, ru, zrn
BU12-182	Kyanite–garnet metapelite	i, s, xg	x	t, r?		x	t		x	ilm, mnz, ru, zrn
BU13-01B	Kyanite–garnet metapelite	i, s	x	t, r?		x			x	ilm, mnz, zrn

<sup>a</sup>All samples contain quartz, biotite and mineral abbreviations are after Whitney & Evans (2010).

<sup>b</sup>Different textural forms of garnet: e, elongate garnet; i, idioblastic garnet; s, subidioblastic garnet; xg, xenoblastic garnet.

<sup>c</sup>Abbreviations include: t, trace amounts; r, retrograde; ?, uncertainty in the presence or stability of a mineral.

<sup>d</sup>K indicates where K-feldspar is dominant over plagioclase.

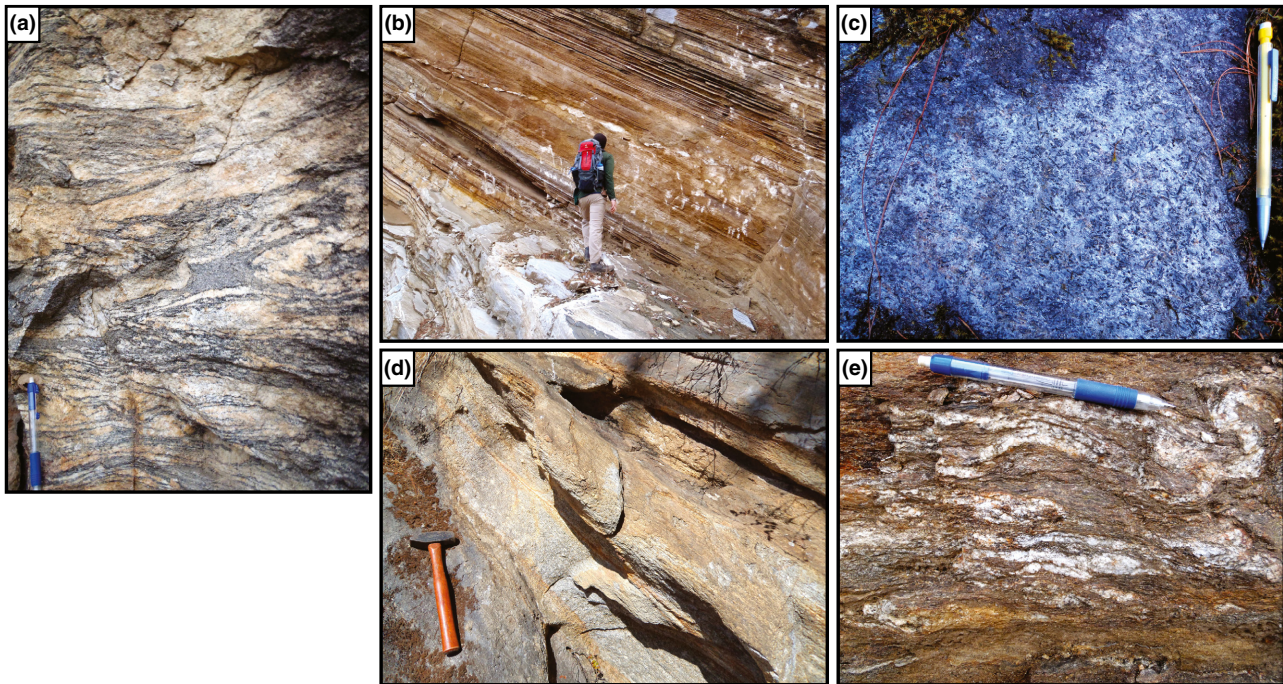


**Fig. 3.** Representative field photographs of different rock types exposed along the two transects: (a) migmatitic metapelite (BU12-198) within the KT zone of the Kuru Chu transect; (b) marble found within the lower-GH of the Bumthang Chu transect; (c) garnet–staurolite schist (BU13-18B) of the Naspe Formation, collected along the Bumthang Chu transect; (d) orthogneiss within the KT zone of the Bumthang Chu transect and (e) sillimanite–garnet metapelite (BU12-212B) lens found within marble in the upper-GH of the Kuru Chu transect.

In north-central Bhutan, the lower-GH consists of interlayered paragneiss and orthogneiss, with a ~0.4 km thick marble body exposed ~6.3 km

structurally above the MCT (Fig. 3b). A distinctive, garnet–staurolite schist, with abundant graphite, is currently exposed at the structurally highest parts of

the lower-GH (Long *et al.*, 2011a); this unit has previously been mapped as the Naspe Formation (Bhargava, 1995; Fig. 3c) or the Chekha Group (Kellett *et al.*, 2010). Kellett *et al.* (2010) also interpreted the basal contact of the Chekha Group on this transect as the outer-STD; however, similar to the northeastern Bhutan transect, we did not observe evidence for a localized shear zone at this contact. We map the garnet–staurolite schist as part of the lower-GH unit. Above the schist, an orthogneiss (Fig. 3d) is exposed, marking the location of the previously mapped KT in north-central Bhutan (Swapp & Hollister, 1991; Grujic *et al.*, 2002).

The lithology of the upper-GH differs between the two transects. In northeastern Bhutan, a body of marble, calc-silicate and quartzite, spanning ~5 km of structural thickness, is found above the migmatitic gneiss (from ~1.3 to 6.8 km above the KT). Metre-scale, sillimanite-bearing metapelites (Fig. 3e) are interlayered within the marble. A *c.* 500 Ma orthogneiss (Zeiger *et al.*, 2015) is exposed at the highest structural level (~6.8 km above the KT) of the northeastern transect. In comparison, the upper-GH in north-central Bhutan mainly consists of migmatitic metapelite and orthogneiss, with only minor quartzite and marble.

Along both transects there is a transition from kyanite in the lower-GH to sillimanite near the KT and in the upper-GH as the dominant aluminosilicate. Moreover, all lithologies reveal a strong macroscopic foliation, typically defined by muscovite, biotite  $\pm$  sillimanite, and exhibit evidence for melt-present deformation where the migmatites are exposed (e.g. melt pooling within shear bands). However, typically the rocks show a weak (or absent) lineation and few kinematic indicators. Petrographic investigations show weak quartz crystallographic-preferred orientations throughout the transects (Penfold *et al.*, 2014). Moreover, there is no evidence of an increase in deformation magnitude near the previously mapped location of the KT on either transect to suggest that a major structure is present.

In contrast to other studied transects of upper-GH rocks within the central and eastern Himalaya (e.g. Ding *et al.*, 2001; Groppo *et al.*, 2010; Kali *et al.*, 2010; Zhang *et al.*, 2010, 2015; Grujic *et al.*, 2011; Guilmette *et al.*, 2011; Warren *et al.*, 2012), there is no observed petrological evidence for the upper-GH rocks having been buried to granulite facies conditions in either of our studied transects. Moreover, where metre-scale mafic pods are exposed within the gneisses, garnet and hornblende are the main components, and orthopyroxene is not observed. This is in contrast to northwestern Bhutan, where orthopyroxene has been documented in the granulitized eclogites and host granulite facies gneisses (Grujic *et al.*, 2011; Warren *et al.*, 2012). In addition, cordierite is not found in samples collected along the two transects. The lack of cordierite in north-central Bhutan is

consistent with the field observations of Swapp & Hollister (1991), who only found cordierite in samples in northwest Bhutan and not in north-central Bhutan. The cordierite was interpreted as evidence for a near-isothermal decompression path for the upper-GH in northwest Bhutan.

## METHODS

Six samples were collected from the Bumthang Chu transect, including a kyanite–garnet metapelite (BU13-01B), a sillimanite-bearing siliceous gneiss (BU13-13A) and a staurolite–garnet schist (BU13-18B) from the lower-GH, and from the upper-GH, a kyanite–sillimanite–garnet metapelite (BU13-23B), a sillimanite-bearing paragneiss (BU13-43A) and an amphibole–garnet orthogneiss (BU13-42B) (Table 1; Figs 2 & 4). In addition, six samples were collected from the Kuru Chu transect, including two kyanite–garnet metapelites from the lower-GH (BU12-182 and BU12-187), and three sillimanite–garnet metapelites (BU12-198, BU12-207A, BU12-212B) and a sillimanite-bearing orthogneiss (BU12-221) from the upper-GH (Table 1; Figs 2 & 5).

Major element mineral compositions and garnet compositional maps were collected using a five-spectrometer Cameca SX-100 electron microprobe at UC-Santa Barbara using synthetic and natural standards for calibration and a ZAF or Phi-Rho-Z matrix correction routine (Armstrong, 1988). Representative garnet grains ( $n = 2\text{--}8$  for 12 samples) were imaged, using qualitative electron dispersive spectroscopy major element maps (Ca, Fe, Mg, Mn) to check for chemical zoning and to guide quantitative wavelength dispersive spectroscopy (WDS) analyses (Figs 6 & 7). Subsequently, WDS analyses on garnet, plagioclase, biotite, muscovite, K-feldspar, staurolite, amphibole and ilmenite were made from core to rim within individual crystals to obtain quantitative spot analyses for thermobarometric calculations, and to also check for zoning (Table S2). Operating conditions for WDS analyses were 15 kV accelerating voltage, 15 nA beam current and 1–2  $\mu\text{m}$  beam size at 20 s peak and 10 s background count times.

For the thermobarometry, minerals in contact were assumed to be in equilibrium. In cases where the matrix minerals were in contact with garnet rims that exhibited significant Mn and Fe# [ $\text{Fe}/(\text{Fe}+\text{Mg})$ ] increases (observed in most samples from this study; Figs 6 & 7), garnet spot analyses at the inner garnet rim (interior to the high Mn and Fe# rims) were paired with the rims of matrix biotite and plagioclase phases to avoid retrograde net transfer reaction effects (e.g. Spear, 1991; Kohn & Spear, 2000). For each sample, multiple mineral combinations were used (i.e. with both adjacent to the garnet and matrix phases) to calculate two to four  $P\text{--}T$  estimates per sample, and results show for most samples that the multiple  $P\text{--}T$  estimates are within error because



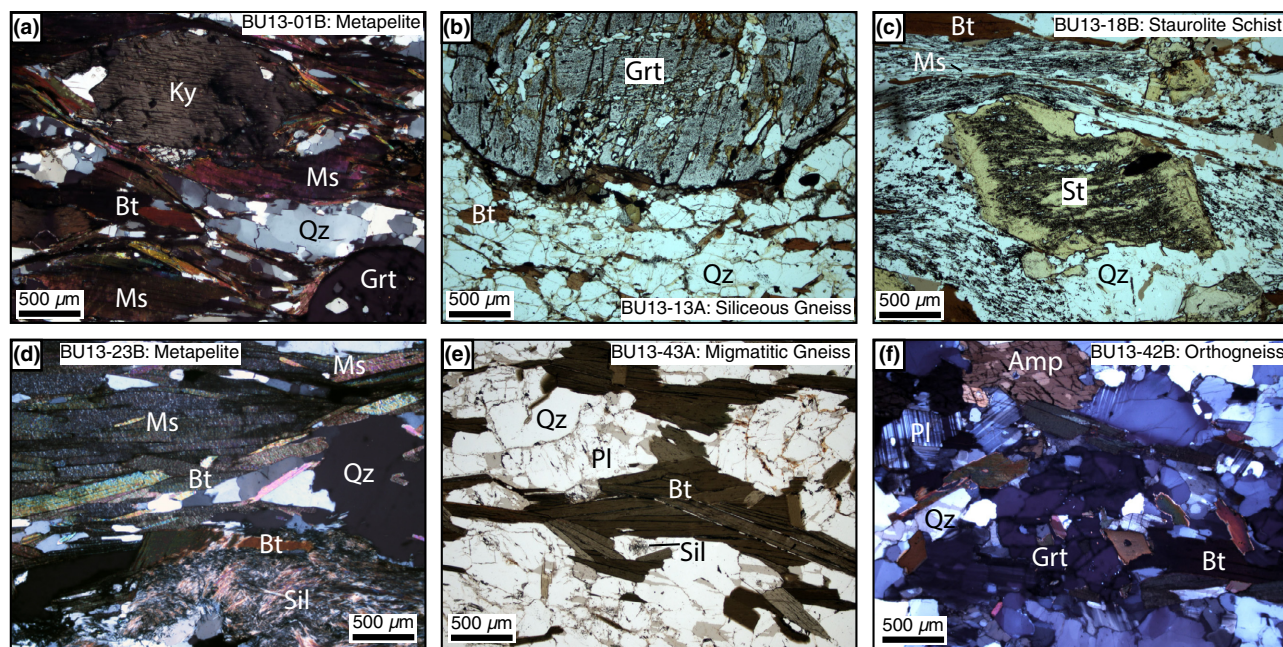


**Fig. 4.** Representative photomicrographs illustrating the mineralogy and textures of samples collected along the Bumthang Chu transect: (a) cross-polarized light (XPL) image of lower-GH metapelite BU13-01B; (b) plane-polarized light (PPL) image of lower-GH siliceous gneiss BU13-13A; (c) PPL image of lower-GH staurolite schist BU13-18B; (d) XPL image of upper-GH metapelite BU13-23B; (e) PPL image of upper-GH migmatitic gneiss BU13-43A and (f) XPL image of upper-GH orthogneiss BU13-42B. Mineral abbreviations after Whitney & Evans (2010).

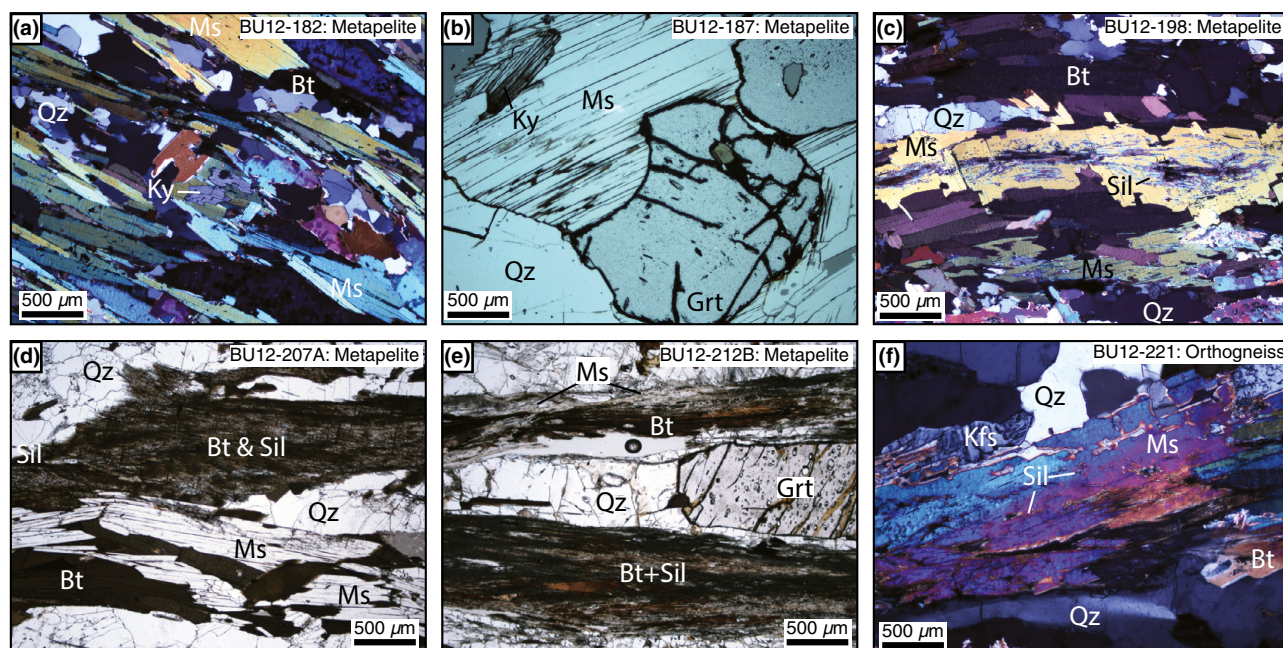


**Fig. 5.** Representative photomicrographs illustrating the mineralogy and textures of samples collected along the Kuru Chu transect: (a) cross-polarized light (XPL) image of lower-GH metapelite BU12-182; (b) plane-polarized light (PPL) image of lower-GH metapelite BU12-187; (c) XPL image of metapelite BU12-198 collected within the KT zone; (d) PPL image of upper-GH metapelite BU12-207A; (e) PPL image of upper-GH metapelite BU12-212B and (f) XPL image of upper-GH orthogneiss BU12-221. Note stable muscovite in all samples. Mineral abbreviations after Whitney & Evans (2010).

biotite and plagioclase compositions throughout these samples were similar regardless of textural location. In samples that contained zoned plagioclase, the

grain rims were used for *P-T* estimates. A summary of representative compositional mineralogy used to calculate *P-T* estimates is presented in Table S1.



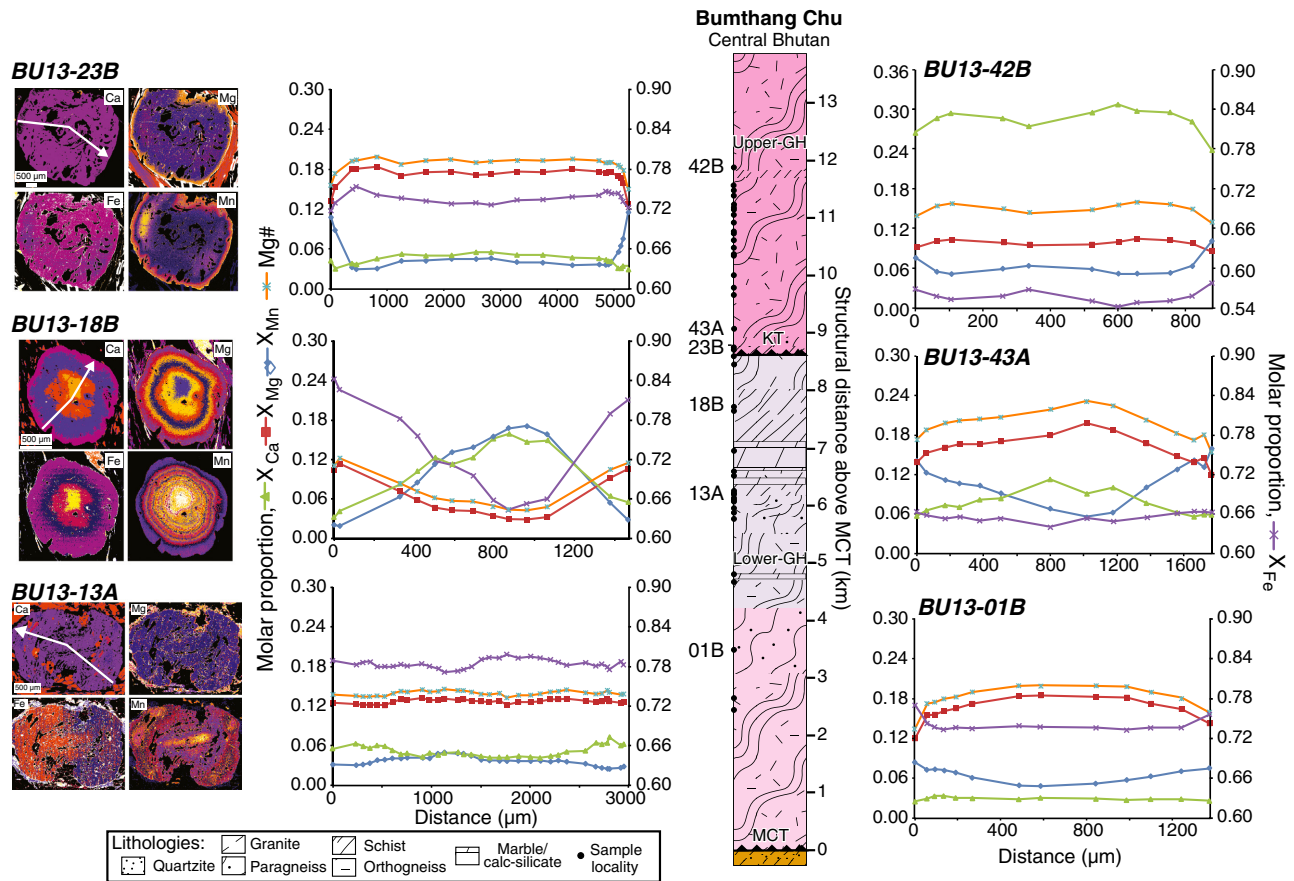


**Fig. 6.** Quantitative mineral profiles and qualitative garnet X-ray compositional maps of representative garnet from samples collected along the Bumthang Chu transect. In the three compositional maps, the lighter/warmer colours correspond to higher concentrations and darker/cooler colours correspond to low concentrations. The white line with arrow in the Ca X-ray map corresponds to the direction of quantitative line scans. For the quantitative mineral profiles, the left axis represents the molar proportion of the Mg# ( $\text{Mg}/(\text{Mg}+\text{Fe})$ ) and three garnet end-members: grossular ( $X_{\text{Ca}}$ ), pyrope ( $X_{\text{Mg}}$ ) and spessartine ( $X_{\text{Mn}}$ ). The right axis represents the molar proportion of garnet end-member almandine ( $X_{\text{Fe}}$ ). Note the extended scale in BU13-42B due to relatively lower molar proportion of almandine. The bottom axis is the distance across the rim-to-rim transect. The structural distance of each sample above the MCT is indicated by the structural column that also shows general lithologies through the GH.

Compositional data (in wt% oxides) were converted into mineral end-member activities via the program AX2 (Holland & Powell, 2003). Garnet–biotite thermometry estimates were calculated using the 5AV model of Holdaway (2000). In addition,  $P$ – $T$  estimates and their respective  $1\sigma$  uncertainties for interpreted minerals in equilibrium were calculated using the internally consistent data set of Holland & Powell (2011; tc-ds62) and THERMOCALC v.3.36 in Average  $P$ – $T$  mode (Powell & Holland, 1988, 1994). THERMOCALC Average  $P$ – $T$  estimates were calculated in two ways: one by fixing the water activity ( $a_{\text{H}_2\text{O}} = 1$ ), and by adjusting the water activity until temperature estimates in THERMOCALC Ave  $P$ – $T$  mode were closest to Holdaway (2000) temperature estimates (e.g. Searle *et al.*, 2003; Jessup *et al.*, 2008; Yakymchuk & Godin, 2012) (Table 2). This study uses the average  $P$ – $T$  estimates with the modified water activities as the best estimate of near-peak  $P$ – $T$  estimates. The

average  $P$ – $T$  estimates and their respective  $1\sigma$  error ellipses for each sample are plotted on a simplified  $P$ – $T$  diagram (Fig. 8).

In upper-GH metapelite BU12-212B, two end-members for albite (from plagioclase and K-feldspar) were generated in AX2. The activities of albite in plagioclase and K-feldspar are 0.92 and 0.82, respectively, and if both were in equilibrium, these should be equal. As K-feldspar is the dominant feldspar in this sample and the use of albite from plagioclase yielded large statistical fit values ( $>2.0$ ) and high absolute values for ( $e^*$ ), the plagioclase albite end-member was removed from all calculations in this sample. In addition, spessartine (Mn-garnet) was automatically removed from all calculations (with exception to amphibole–garnet orthogneiss BU13-42B) due to a lack of other Mn-bearing end-members at peak  $P$ – $T$  conditions in this study. Furthermore, to more accurately compare the previous  $P$ – $T$



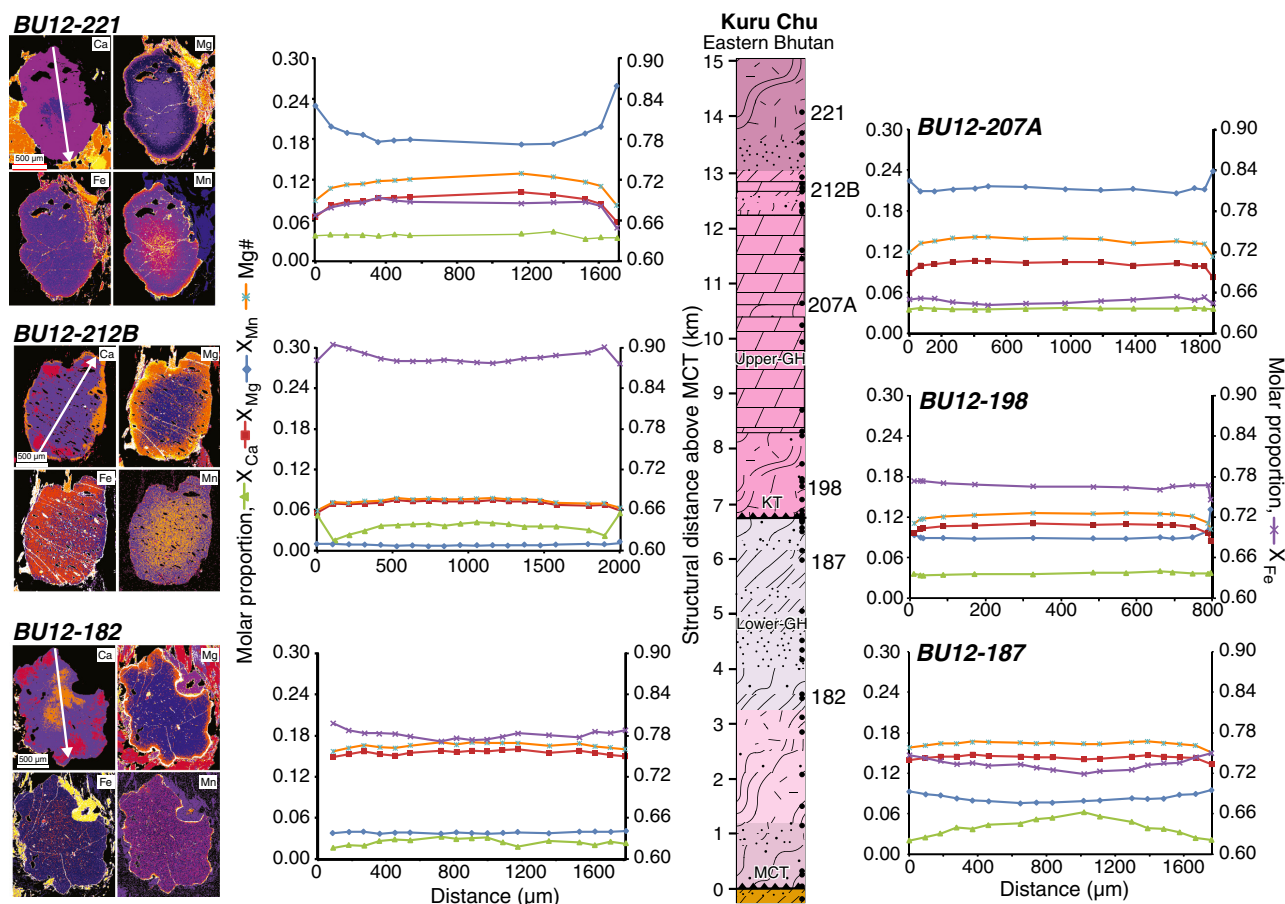


Fig. 7. Quantitative mineral profiles and qualitative garnet X-ray compositional maps of representative garnet from samples collected along the Kuru Chu transect. Abbreviations and labels are identical to Fig. 6.

estimates to those in this study, data from Daniel *et al.* (2003) were recalculated using the methods from this study.

Temperature estimates were also calculated using the Ti-in-biotite thermometer (Henry *et al.*, 2005) to complement peak-temperature estimates determined in THERMOCALC (Fig. 9). The Ti-in-biotite thermometer is optimized for metapelites equilibrated at 4–6 kbar. For all samples, individual spot analyses of biotite included in garnet and biotite in the matrix and adjacent to garnet were analysed for Ti. The Ti in biotite is reported in atoms per formula unit (apfu) (Table S3). All samples satisfy the requirements for the Ti-in-biotite thermometer (Henry *et al.*, 2005), including the presence of: ilmenite or rutile, graphite, quartz, aluminosilicates and biotite with a specific compositional range ( $X_{\text{Mg}} = 0.275\text{--}1.000$  and  $\text{Ti} = 0.04\text{--}0.60$  apfu).

Titanium-in-biotite temperatures from differing biotite textural locations (e.g. garnet inclusions *v.* in the matrix) can provide insight into the prograde-to-peak temperature path; however, there are a few limitations to the thermometer. For example, biotite in direct contact with garnet will typically yield the

lowest and highest Ti-temperature estimates for each sample. Henry *et al.* (2005) suggested that the low temperatures result from distinct local Ti or Mg/(Fe+Mg) depletion, whereas the high temperatures may be the result of compositional resetting of biotite and not necessarily indicative of peak-temperature conditions. Matrix biotite within most samples is zoned, and the highest temperature estimates are recorded at the biotite rims. Most of the biotite rims are distal to other ferromagnesian and Ti-bearing minerals and thus are less likely to have anomalous temperature estimates (Henry *et al.*, 2005); therefore, the matrix biotite rims are interpreted to provide the best peak Ti-in-biotite temperature estimates. Moreover, biotite included in garnet that was not adjacent to cracks or rutile likely gives insight into the prograde temperature path for these rocks.

The Ti-in-biotite temperature results are reported in Table S3 and Fig. 9. For samples that equilibrated at pressures above which this thermometer is optimized (4–6 kbar), the temperatures are considered minimum estimates. Although uncertainties of the Ti-in-biotite thermometer are  $\pm 24^\circ\text{C}$  at  $<600^\circ\text{C}$  and  $\pm 12^\circ\text{C}$  at  $>700^\circ\text{C}$  (Henry *et al.*, 2005), a more

**Table 2.** Average pressure–temperature estimates for the central and eastern Bhutan samples analysed via THERMOCALC<sup>a</sup>.

Sample <sup>b</sup>	Latitude	Longitude	Approximate structural distance above:		T (°C)		Water activity		T (°C)	1 $\sigma$ (°C)	P (kbar)	1 $\sigma$ (kbar)	Correlation	Sigma fit	n <sup>d</sup>	End-member removed <sup>e</sup>
			MCT (km)	KT (km)	Holdaway (2000)	Assemblage <sup>c</sup>	$\alpha$ (H <sub>2</sub> O)	$\alpha$ (H <sub>2</sub> O)								
BU13-01B_G1	27.550889	90.758028	3.4	−5.2	671	Grt, Bt, Ms, Pl, Ky	1.00	1.00	759	29	9.4	1.3	0.794	0.68	7	—
BU13-01B_G2						Grt, Bt, Ms, Pl, Ky	0.60	0.60	679	25	8.9	1.2	0.787	0.70	—	—
BU13-01B_G3						Grt, Bt, Ms, Pl, Ky	1.00	1.00	759	30	9.1	1.3	0.795	0.38	7	—
						Grt, Bt, Ms, Pl, Ky	0.60	0.60	679	26	8.6	1.2	0.787	0.55	—	—
BU12-182_G2	27.673000	91.182917	3.5	−3.2	660	Grt, Bt, Ms, Pl, Ky	1.00	1.00	740	28	9.0	1.2	0.814	0.61	7	—
BU12-182_G6						Grt, Bt, Ms, Pl, Ky	0.60	0.60	662	24	8.5	1.1	0.808	0.57	—	—
						Grt, Bt, Ms, Pl, Ky	1.00	1.00	778	31	9.6	1.3	0.758	0.91	7	—
						Grt, Bt, Ms, Pl, Ky	0.50	0.50	671	25	9.0	1.1	0.749	0.97	—	—
						Grt, Bt, Ms, Pl, Ky	1.00	1.00	760	29	9.5	1.3	0.803	0.94	7	—
						Grt, Bt, Ms, Pl, Ky	0.50	0.50	659	26	9.2	1.3	0.794	1.11	—	—
BU12-187_G1	27.712028	91.158000	6.0	−0.7	704	Grt, Bt, Ms, Pl, Ky	1.00	1.00	748	30	8.3	1.3	0.802	0.98	7	—
BU12-187_G2						Grt, Bt, Ms, Pl, Ky	0.75	0.75	705	28	8.2	1.3	0.798	0.94	—	—
BU12-187_G3						Grt, Bt, Ms, Pl, Ky	1.00	1.00	763	37	8.2	1.4	0.758	1.13	7	—
						Grt, Bt, Ms, Pl, Ky	0.75	0.75	719	32	8.1	1.3	0.755	1.09	—	—
						Grt, Bt, Ms, Pl, Ky	1.00	1.00	742	29	8.4	1.3	0.803	0.85	7	—
BU13-13A_G1	27.653917	90.747028	6.2	−2.4	614	Grt, Bt, Ms, Pl, Sil	0.75	0.75	699	27	8.2	1.2	0.799	0.82	—	—
BU13-13A_G3						Grt, Bt, Ms, Pl, Sil	1.00	1.00	730	33	8.4	1.2	0.885	0.99	5	—
						Grt, Bt, Ms, Pl, Sil	0.40	0.40	609	26	7.4	1.1	0.880	0.49	—	—
						Grt, Bt, Ms, Pl, Sil	1.00	1.00	729	33	8.4	1.2	0.889	0.80	5	—
BU12-198_G1	27.746472	91.129389	7.3	0.6	676	Grt, Bt, Ms, Pl, Sil	0.40	0.40	608	26	7.4	1.1	0.884	0.40	—	—
BU12-198_G2						Grt, Bt, Ms, Pl, Sil	1.00	1.00	756	40	6.9	1.2	0.824	0.57	7	—
BU12-198_G3						Grt, Bt, Ms, Pl, Sil	0.60	0.60	684	35	6.5	1.1	0.821	0.42	—	—
						Grt, Bt, Ms, Pl, Sil	1.00	1.00	753	39	6.9	1.2	0.826	0.41	7	—
						Grt, Bt, Ms, Pl, Sil	0.60	0.60	682	34	6.5	1.1	0.823	0.22	—	—
						Grt, Bt, Ms, Pl, Sil	1.00	1.00	746	39	6.8	1.1	0.825	0.35	7	—
						Grt, Bt, Ms, Pl, Sil	0.60	0.60	674	34	6.4	1.1	0.822	0.30	—	—
BU13-18B_G1	27.688333	90.723278	7.7	−0.9	615	Grt, Bt, Ms, Pl, St, Sil	1.00	1.00	674	23	7.0	1.0	0.936	0.88	9	—
BU13-18B_G4						Grt, Bt, Ms, Pl, St, Sil	0.50	0.50	610	20	7.0	1.0	0.932	0.71	—	—
						Grt, Bt, Ms, Pl, St, Sil	1.00	1.00	665	23	6.6	1.0	0.936	0.77	9	—
						Grt, Bt, Ms, Pl, Ky, Sil	0.50	0.50	600	20	6.5	0.9	0.933	0.55	—	—
BU13-23B_G1	27.700611	90.730583	8.7	60 m	645	Grt, Bt, Ms, Pl, Ky, Sil	1.00	1.00	739	30	8.5	0.7	0.980	0.82	8	—
BU13-23B_G5						Grt, Bt, Ms, Pl, Ky, Sil	0.60	0.60	650	26	6.7	0.6	0.973	0.68	—	—
						Grt, Bt, Ms, Pl, Ky, Sil	1.00	1.00	735	29	8.4	0.6	0.978	0.73	8	—
						Grt, Bt, Ms, Pl, Ky, Sil	0.60	0.60	646	24	6.6	0.5	0.970	0.68	—	—
BU13-43A_G1	27.705306	90.731917	8.9	0.3	679	Grt, Bt, Pl, Sil	1.00	1.00	702	131	9.0	2.3	0.850	0.12	3	—
BU13-43A_G3						Grt, Bt, Pl, Sil	1.00	1.00	715	135	8.5	2.3	0.836	0.04	3	—
BU13-43A_G6						Grt, Bt, Pl, Sil	1.00	1.00	716	135	9.0	2.3	0.847	0.09	3	—
BU12-207A_G1	27.803000	91.102833	10.6	3.9	661	Grt, Bt, Ms, Pl, Sil	1.00	1.00	747	42	6.1	1.2	0.810	0.52	7	—
BU12-207A_G4						Grt, Bt, Ms, Pl, Sil	0.60	0.60	678	37	5.8	1.1	0.805	0.41	—	—
						Grt, Bt, Ms, Pl, Sil	1.00	1.00	718	38	6.0	1.1	0.832	0.57	7	—
						Grt, Bt, Ms, Pl, Sil	0.60	0.60	653	33	5.7	1.1	0.828	0.57	—	—
BU12-207A_G5						Grt, Bt, Ms, Pl, Sil	1.00	1.00	730	39	5.9	1.1	0.819	0.66	7	—
						Grt, Bt, Pl, Amp, Ilm, Spn	0.60	0.60	664	34	5.7	1.1	0.814	0.67	—	—
BU13-42B_G1	27.763194	90.721056	11.8	3.2	665	Grt, Bt, Pl, Amp, Ilm, Spn	1.00	1.00	784	78	9.4	1.0	0.651	1.11	9	—
BU13-42B_G2						Grt, Bt, Pl, Amp, Ilm, Spn	0.20	0.20	687	80	7.9	1.1	0.579	1.39	—	—
BU13-42B_G4						Grt, Bt, Pl, Amp, Ilm, Spn	1.00	1.00	779	81	9.4	1.1	0.662	1.14	9	—
						Grt, Bt, Pl, Amp, Ilm, Spn	0.20	0.20	684	81	7.9	1.1	0.590	1.40	—	—
BU12-212B_G1	27.834167	91.115222	12.4	5.7	639	Grt, Bt, Ms, Pl, Afs, Sil	1.00	1.00	770	79	9.6	1.1	0.649	1.17	9	—
BU12-212B_G2						Grt, Bt, Ms, Pl, Afs, Sil	0.40	0.40	647	24	7.1	1.1	0.899	0.73	8	ab (pl)
						Grt, Bt, Ms, Pl, Afs, Sil	1.00	1.00	760	40	7.4	1.6	0.903	1.29	8	ab (pl)



Table 2. (Continued)

Sample <sup>b</sup>	Latitude	Longitude	Approximate structural distance above:		Assemblage <sup>c</sup>	T (°C)		Water activity	T (°C)	1σ (°C)	P (kbar)	1σ (kbar)	Correlation	Sigma fit	n <sup>d</sup>	End-member removed <sup>e</sup>
			MCT (km)	KT (km)		Holdaway (2000)	a(H <sub>2</sub> O)									
BU12-212B_G4					Grt, Bt, Ms, Pl, Afs, Sil		0.40		634	29	6.7	1.4	0.898	1.28	8	ab (pl)
							1.00		780	32	8	1.3	0.895	0.79		
BU12-212B_G5					Grt, Bt, Ms, Pl, Afs, Sil		0.40		650	24	7.2	1.1	0.892	0.66	8	ab (pl)
							1.00		783	33	7.9	1.3	0.901	0.46		
							0.40		653	24	7.1	1.1	0.898	0.47		
BU12-221_G1	27.882278	91.123472	14.0	7.4	Grt, Bt, Ms, Pl, Sil	699	1.00		773	43	6.0	1.1	0.770	0.91	7	–
							0.60		705	39	5.7	1.0	0.766	0.93		
BU12-221_G2					Grt, Bt, Ms, Pl, Sil		1.00		774	45	5.8	1.1	0.773	0.92	7	–
							0.60		705	40	5.5	1.0	0.769	0.86		
BU12-221_G4					Grt, Bt, Ms, Pl, Sil		1.00		783	47	6.4	1.2	0.759	1.12	7	–
							0.60		716	48	6.2	1.3	0.754	1.27		

<sup>a</sup>All calculations are for  $X_{H_2O} = 1$  (see methods).<sup>b</sup>Sample number includes the garnet crystal used to calculate results.<sup>c</sup>Mineral abbreviations after Whitney & Evans (2010).<sup>d</sup>The *n* = number of independent reactions used to calculate the pressures and temperatures.<sup>e</sup>Spessartine was automatically removed in all calculations except for sample BU13-42B.

conservative uncertainty of  $\pm 24$  °C was applied to all samples.

Pressure–temperature–structural distance regression lines were calculated using a robust regression in ISO-PLOT (v.4.15; Ludwig, 2008). A conservative uncertainty ( $\pm 100$  m) was applied to the location of each sample within the structural column. ISO-PLOT incorporates the individual errors in pressure estimates and location into the slope calculation of the regression lines.

## SAMPLE PETROGRAPHY AND MINERAL CHEMISTRY

A summary of the mineralogy for all samples is presented in Table 1, and average mineral compositions are reported in Tables 2 and S1. All samples are discussed below sequentially from the structurally lowest to the structurally highest sample for each transect (Fig. S1). Approximate structural positions of the samples with respect to each other, to the MCT and the KT were determined from field measurements and from cross-sections (Fig. S1). As the MCT was not observed on the Bumthang Chu transect, the structural level of the MCT in the subsurface was taken from Long *et al.* (2011b).

### Bumthang Chu lower-GH samples

The structurally lowest sample from the Bumthang Chu transect, BU13-01B (3.4 km above the MCT and 5.2 km below the KT) is a kyanite–garnet metapelite (+ minor ilmenite and trace fibrolite) collected from a massive outcrop of metapelite near the town of Jakar (Figs 2, 4a & 6). Layers of oriented biotite, muscovite and kyanite alternating with ribbons mainly of quartz with minor plagioclase define a strong foliation (Fig. 4a). Garnet grains are idioblastic to subidioblastic, up to 2 mm in diameter, and contain abundant inclusions of biotite, muscovite and quartz. All crystals exhibit uniform grossular ( $X_{Ca} = 0.03$ ), whereas spessartine and Fe# increase from core ( $X_{Mn} = 0.05$ ; Fe# = 0.80) to rim ( $X_{Mn} = 0.08$ ; Fe# = 0.85) (Fig. 6). Matrix biotite shows little variation in Fe# (0.50–0.52) and a Ti range 0.11–0.16 apfu. In contrast, biotite inclusions in garnet have lower Fe# (0.40–0.42) and consistently lower Ti (0.11–0.12 apfu). Plagioclase crystals are unzoned (An<sub>13–14</sub>). Muscovite adjacent to garnet has higher Fe# (~0.46–0.48) at garnet rims and lower Fe# (~0.43–0.45) >100  $\mu$ m away from the rims, whereas muscovite in the remaining matrix shows little zoning (Fe# = 0.42–0.44). Kyanite is abundant and typically forms large laths (50 mm) that are oriented parallel to the foliation (Fig. 4a).

Sample BU13-13A, located 6.2 km above the MCT and 2.4 km below the KT, is a siliceous, garnet-bearing gneiss, with minor sillimanite, collected from an

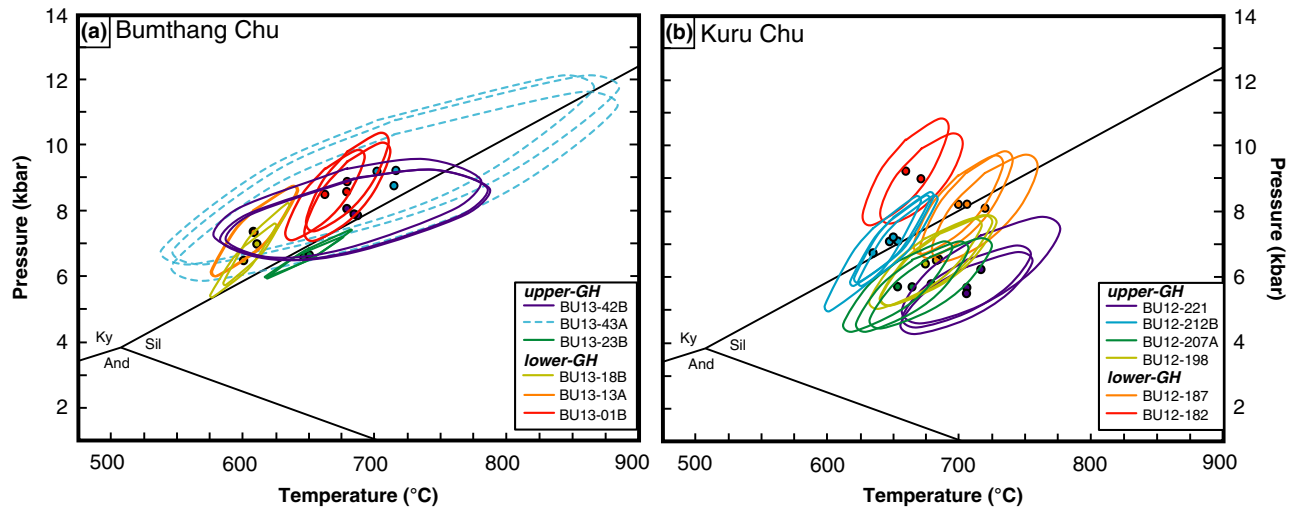


Fig. 8. Pressure–temperature results calculated from THERMOCALC for the (a) Bumthang Chu transect and (b) Kuru Chu transect.

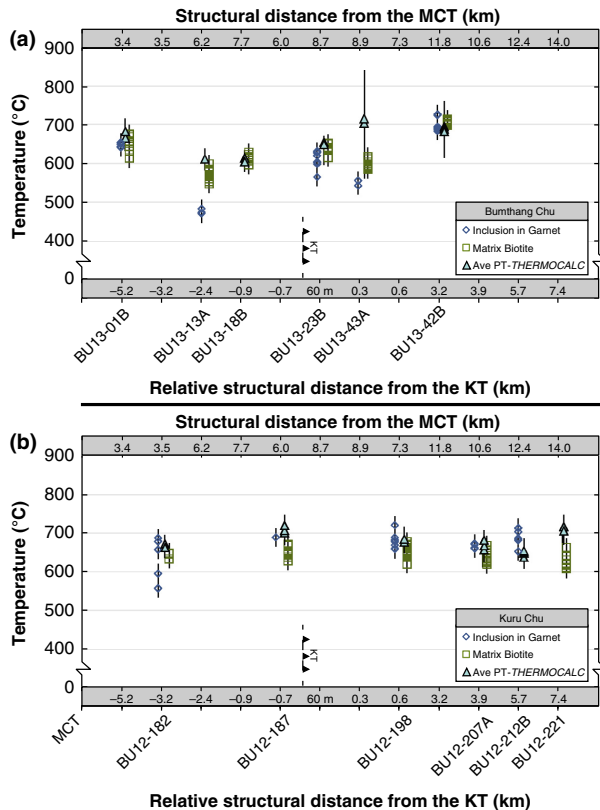


Fig. 9. Titanium-in-biotite temperature estimates and uncertainties for biotite inclusions in garnet and for matrix biotite plotted v. structural distance relative to the KT and MCT; the Ti-in-biotite temperatures are considered minimum-temperature estimates. Samples are ordered in increasing structural distance above the KT and are separated by transect: a) Bumthang Chu and b) Kuru Chu. The relative position of the KT is shown for reference. Each Ti-in-biotite data point is a single analysis with a  $\pm 24$  °C error. Temperature estimates determined via Average PT mode in THERMOCALC are also shown for comparison.

outcrop of interlayered schist, paragneiss and orthogneiss (Figs 2, 4b & 6). Biotite and minor muscovite form a weak foliation. The garnet is subidioblastic and up to 3 mm in diameter (Figs 4a & 6). Abundant inclusions of quartz, plagioclase and biotite in the garnet core define sinuous inclusion trails. Garnet displays weak chemical zoning (Fig. 6). Spessartine is highest in the core ( $X_{Mn} = 0.05$ ) and lowest 100  $\mu m$  inside the rim ( $X_{Mn} = 0.03$ ). Grossular exhibits the opposite trend ( $X_{Ca}$  rim = 0.07;  $X_{Ca}$  mantle = 0.04;  $X_{Ca}$  core = 0.05), whereas Fe# slightly varies (0.87–0.85). Biotite shows no Fe# or Ti zonation, but has different compositions depending on textural location. Biotite in the garnet pressure shadows and adjacent to garnet exhibits the highest Fe# (~0.60), matrix biotite >100  $\mu m$  from garnet rims has lower Fe# (0.52–0.55) and inclusions in garnet have the lowest Fe# (0.39–0.43). Biotite adjacent to garnet has a Ti range 0.12–0.21 apfu, matrix grains have a narrow Ti range (0.17–0.20 apfu) and inclusions within garnet have low Ti (0.02–0.06 apfu). Anorthite in matrix plagioclase shows minimal zoning between cores (~An<sub>21–23</sub>) and rims (~An<sub>21–25</sub>). Plagioclase inclusions in garnet cores have higher Ca (An<sub>26–28</sub>). Muscovite crystals adjacent to garnet have higher Fe# at the garnet rim (0.62–0.64) in comparison to ~50  $\mu m$  from the rim (0.53–0.58). Muscovite inclusions within garnet have similar Fe# (0.52–0.57) compared to the matrix muscovite. Sillimanite is present as small (~200  $\mu m$ ) isolated clusters of fibrolite. In addition, tourmaline is found throughout the sample.

Sample BU13-18B is a garnet–staurolite schist with minor sillimanite from the Naspe Formation (Bhargava, 1995), ~8.0 km above the MCT and 0.85 km below the KT (Figs 2, 4c & 6). Biotite, muscovite, graphite and minor sillimanite layers alternate with quartz and plagioclase-rich layers to define a strong foliation. Garnet is idioblastic to subidioblastic, up to



2 mm in diameter, and contains sparse inclusions of plagioclase and ilmenite. Garnet has well-preserved zoning with decreasing spessartine and grossular from core ( $X_{\text{Mn}} = 0.17$ ;  $X_{\text{Ca}} = 0.15$ ) to rim ( $X_{\text{Mn}} = 0.02$ ;  $X_{\text{Ca}} = 0.04$ ) (Fig. 5). Smaller (600  $\mu\text{m}$ ) garnet grains have less pronounced profiles with a decrease in Fe# and grossular from core (Fe# = 0.96;  $X_{\text{Ca}} = 0.07$ ) to rim (Fe# = 0.89;  $X_{\text{Ca}} = 0.04$ ). Small inclusions of graphite and quartz are found in the cores of garnet and staurolite but not in the inclusion-absent rims (Fig. 4c). Large (up to 4 mm) idioblastic staurolite grains typically contain abundant quartz inclusions and are typically elongate parallel to the foliation plane. Inclusion-poor staurolite rims have lower Fe# (0.84) relative to the inclusion-rich core (0.86). Biotite in the matrix and adjacent to garnet shows no discernable Fe# (0.57–0.59) or Ti (0.20–0.26 apfu) zoning. Muscovite in the matrix shows subtle zoning in Fe# from core (~0.49) to rim (~0.51), but matrix grains adjacent to garnet grains vary more in Fe# (0.48–0.66) and are unzoned. Plagioclase in the matrix and adjacent to garnet shows similar core ( $\text{An}_{19}$ ) and rim ( $\text{An}_{20}$ ) values, whereas plagioclase inclusions in garnet are significantly higher in Ca ( $\text{An}_{35}$ ). Sillimanite is rare and where observed exists as fibrolite needles aligned within the foliation plane.

#### Bumthang Chu upper-GH samples

Sample BU13-23B is a migmatitic kyanite–sillimanite–garnet metapelite (+ minor ilmenite) collected ~60 m and 8.5 km above the KT and MCT, respectively (Figs 2, 4d & 6). This migmatitic metapelite contains small pockets of quartzofeldspathic material, interpreted as crystallized melt, and in addition, a folded, layer-parallel leucosome is found in the outcrop (Zeiger *et al.*, 2015). Oriented biotite, muscovite  $\pm$  sillimanite mark the foliation (Fig. 4d). Garnet grains are subidioblastic, up to 2.5 mm in length, and commonly elongate parallel to the foliation plane. Most garnet grains contain abundant quartz and minor biotite and opaque inclusions. Some garnet grains contain rutile needle inclusions in the rim, and spiral inclusion trails of quartz in the core. All garnet grains display weak zonation profiles with a large increase in Mn and Fe# at the rim (Fig. 6). Spessartine, grossular and Fe# decrease from core ( $X_{\text{Mn}} = 0.04$ ;  $X_{\text{Ca}} = 0.06$ ; Fe# = 0.81) to ~500  $\mu\text{m}$  interior of the rim ( $X_{\text{Mn}} = 0.03$ ;  $X_{\text{Ca}} = 0.04$ ; Fe# = 0.80). Biotite crystals adjacent to garnet have a range of Fe# (0.49–0.55) and Ti values (0.15–0.28 apfu), whereas matrix biotite grains have Fe# of 0.50–0.52 and Ti of 0.25–0.28. Biotite inclusions within garnet cores have Fe# of 0.36–0.38 and Ti of 0.14–0.17 apfu, whereas those within the garnet mantle have Fe# of 0.45–0.47 and Ti of 0.22–0.23 apfu. Matrix plagioclase grains show an increase in Ca from core to rim ( $\text{An}_{23-26}$ ,  $\text{An}_{27-30}$ , respectively). Matrix muscovite has Fe# of 0.38–0.54, whereas

inclusions in garnet have Fe# that ranges from 0.37 to 0.52; all muscovite is unzoned. Kyanite is bladed, up to 1.5 mm in length, and typically found associated with muscovite grains. Sillimanite is observed as fibrolitic mats within or adjacent to zones of biotite and muscovite (Fig. 5d).

Migmatitic garnet gneiss sample, BU13-43A, was collected 0.3 km and 8.9 km above the KT and MCT, respectively (Figs 2 & 6). Biotite defines a weak foliation (Fig. 5e). Garnet grains are subidioblastic, up to 2 mm in diameter, and contain small inclusions of biotite, plagioclase and quartz. Spessartine and Fe# gradually increase from core ( $X_{\text{Mn}} = 0.03$ ; Fe# = 0.76) to rim ( $X_{\text{Mn}} = 0.14$ ; Fe# = 0.82), and grossular decreases from core ( $X_{\text{Ca}} = 0.11$ ) to rim ( $X_{\text{Ca}} = 0.06$ ) (Fig. 6). Matrix biotite exhibits subtle Fe# zonation from core (0.49–0.51) to rim (0.47–0.49). Titanium in biotite is unzoned and ranges from 0.07 to 0.11 apfu. Matrix plagioclase is zoned, with Ca decreasing from core ( $\text{An}_{41}$ ) to rim ( $\text{An}_{32}$ ). Sillimanite is present as small <100  $\mu\text{m}$  fibrolitic clusters.

Sample BU13-42B is an amphibole–biotite–garnet orthogneiss (+ ilmenite and titanite) interlayered within an outcrop dominated by migmatitic paragneiss, 3.2 km and 11.8 km above the KT and MCT, respectively (Figs 2, 4f & 6). Amphibole and biotite define a weak foliation. Garnet is subidioblastic to xenoblastic, up to 1 mm in diameter, and contains biotite, quartz and plagioclase inclusions. In addition, garnet is weakly zoned, with grossular decreasing from core ( $X_{\text{Ca}} = 0.32$ ) to rim ( $X_{\text{Ca}} = 0.24$ ) (Fig. 6). Spessartine and Fe# increase from core ( $X_{\text{Mn}} = 0.05$ ; Fe# = 0.86) to rim ( $X_{\text{Mn}} = 0.10$ ; Fe# = 0.89). Matrix biotite is unzoned and has Fe# of 0.54–0.56 and Ti of 0.20–0.21 apfu, whereas biotite inclusions within garnet have a larger range of Fe# (0.49–0.58) and Ti (0.18–0.22). Plagioclase is abundant, and matrix plagioclase grains have lower Ca ( $\text{An}_{40-47}$ ) than plagioclase adjacent to garnet ( $\text{An}_{50-65}$ ). Amphibole grains are unzoned and have Fe# of 0.58–0.60. Ilmenite is present as wormy growths with quartz, is often found in contact with titanite, and ranges in Fe from 0.94 to 0.98 apfu (3-oxygen basis).

#### Kuru Chu lower-GH samples

Sample BU12-182 is a kyanite–garnet metapelite (+ minor chlorite and ilmenite) collected within a mica-rich schist outcrop that contained layer-parallel leucosomes. This metapelite is the structurally lowest sample (3.5 km above the MCT and 3.2 km below the KT) from the Kuru Chu transect (Figs 2 & 7). Biotite- and muscovite-rich layers alternating with quartzofeldspathic ribbons mark a strong foliation (Fig. 5a). Garnet is typically subidioblastic to xenoblastic. The subidioblastic garnet is up to 2 mm in diameter and contains minor inclusions of biotite, quartz and rutile within grain cores (rims are inclusion free), whereas the xenoblastic garnet is typically

fractured and elongate (up to 2.5 mm) parallel to foliation. The majority of both populations exhibit a slight increase in  $X_{Ca}$  (from 0.02 to 0.03) and  $X_{Mn}$  (from 0.04 to 0.06) at the garnet rims (Fig. 7). Garnet Fe# (~0.83) is unzoned, with some grains exhibiting an increase at the rim (~0.88). Matrix biotite shows little variation in Fe# (~0.55–0.58), whereas inclusions in garnet have a lower Fe# (0.42–0.47). Biotite adjacent to garnet shows variability in Ti (0.15–0.34 apfu). In comparison, biotite in the matrix and as inclusions in garnet has relatively moderate Ti (0.27–0.31 apfu). Plagioclase adjacent to garnet is relatively enriched in Ca ( $An_{16}$ ) compared to matrix grains, which have an undefined zoning pattern (core =  $An_{12-13}$ , rim =  $An_{13-15}$ ). Matrix plagioclase rims were used in  $P$ – $T$  estimates for this sample. Muscovite in the matrix exhibits Fe# zoning, with higher Fe# (~0.47) at the rim compared to the core (~0.40), and muscovite directly adjacent to garnet has a higher Fe# (~0.49). Kyanite is in relatively low abundance as relatively small (400  $\mu$ m) blades.

Sample BU12-187 is a coarse-grained kyanite–garnet metapelite (+ minor chlorite, ilmenite, tourmaline and minor sillimanite) collected directly above a massive quartzite body, 6.0 km above the MCT and 0.7 km below the KT (Figs 2, 5b & 7). Muscovite and biotite define the foliation. Garnet is predominately idioblastic to subidioblastic, up to 2 mm in diameter with minor inclusions of biotite and quartz in grain cores. Garnet shows a weak  $X_{Ca}$  zoning pattern, with higher cores ( $X_{Ca}$  = 0.06) and lower rims ( $X_{Ca}$  = 0.02) (Fig. 6). Spessartine and Fe# show the opposite pattern, with increasing  $X_{Mn}$  and Fe# from core (0.08 and 0.83, respectively) to rim (0.10 and 0.85, respectively) for larger (2 mm in diameter) garnet grains, whereas smaller (1 mm in diameter) crystals show consistent  $X_{Mn}$  of 0.10. Matrix biotite exhibits slight variation in Fe# from core (0.58) to rim (0.61), with the highest value in biotite adjacent to garnet (0.62). In contrast, Ti in matrix biotite shows the opposite trend from core (0.33 apfu) to rim (0.31 apfu), with the lowest Ti adjacent to garnet (0.27 apfu). Matrix plagioclase is unzoned and ranges from  $An_{10-14}$ . Muscovite is the dominant mica in this sample, and its Fe# ranges from 0.45 to 0.48, with Fe# typically highest where the grains are adjacent to biotite. Kyanite blades are small, up to 500  $\mu$ m in length, and are typically located within zones of muscovite, whereas trace fibrolite is also observed within zones of muscovite.

### Kuru Chu upper-GH samples

Sample BU12-198 is a migmatitic sillimanite–garnet metapelite (+ ilmenite) collected 0.6 km and 7.3 km above the KT and MCT, respectively (Figs 2, 3c & 7). This outcrop, including other migmatites ~0.5 km structurally below, marks a noticeable increase in the volume percentage of leucosomes exposed, from

<~10% in similar metapelites exposed in the lower-GH to >~30% in outcrop BU12-198. However, a large quartzite body separates the metapelites and thus makes it difficult to assess if the increase in leucocratic material is abrupt or gradual. Biotite, muscovite and sillimanite define a strong foliation in the BU12-198 metapelite (Fig. 5c). Two types of garnet are found: (i) idioblastic garnet is relatively small (<1 mm); and (ii) subidioblastic garnet is elongate and up to 1.3 mm. Grossular is relatively constant at  $X_{Ca}$  = 0.04, whereas  $X_{Mn}$  and Fe# increase slightly from the mantle ( $X_{Mn}$  = 0.09; Fe# = 0.88) to rim ( $X_{Mn}$  = 0.11; Fe# = 0.90) across both types. Matrix biotite is unzoned and has Fe# ranging from 0.64 to 0.67, whereas inclusions in garnet have slightly lower Fe# of 0.57–0.59. Titanium in all biotite ranges from 0.13 to 0.19 apfu. Plagioclase adjacent to garnet exhibits no apparent Ca zonation ( $An_{21-23}$ ), whereas matrix plagioclase exhibits an increase in Ca from rim ( $An_{18}$ ) to core ( $An_{22}$ ). Muscovite in the matrix is unzoned and has Fe# that ranges from 0.53 to 0.64. Sillimanite is present as fibrolitic mats primarily within muscovite grains (Fig. 5c).

Sillimanite–garnet metapelite (+ ilmenite and tourmaline), BU12-207A, is from an outcrop that also includes an intrusive sill of quartzofeldspathic, layer-parallel leucosome with cusped margins (Zeiger *et al.*, 2015), 3.9 km and 10.6 km above the KT and MCT, respectively (Figs 2 & 7). Primarily biotite and sillimanite with lesser muscovite outline a strong foliation (Fig. 5d). Garnet is idioblastic to elongate, fractured and contains few inclusions of quartz, biotite and plagioclase. Idioblastic garnet is up to 0.6 mm in diameter, whereas elongate grains are up to 2 mm in length. Grossular decreases from core ( $X_{Ca}$  = 0.05) to rim ( $X_{Ca}$  = 0.04), whereas spessartine and Fe# increase from the mantle (~100  $\mu$ m from the garnet rim;  $X_{Mn}$  = 0.20; Fe# = 0.85) to the rim ( $X_{Mn}$  = 0.22; Fe# = 0.87) (Fig. 7). Matrix biotite has slightly higher Fe# at the rim (0.58–0.59) compared to the core (0.57–0.58). In contrast, biotite adjacent to garnet has slightly higher Fe# (0.59–0.62). Biotite shows no Ti zoning, but differences among textural locations. Biotite adjacent to garnet has a range of Ti values (0.14–0.24 apfu), whereas matrix crystals range from 0.12 to 0.15 apfu. Matrix plagioclase is zoned, with increasing Ca from the rim ( $An_{23-25}$ ) to the core ( $An_{25-29}$ ). Plagioclase adjacent to garnet has lower Ca ( $An_{21-25}$ ) than plagioclase >100  $\mu$ m from the garnet rim ( $An_{27-34}$ ), and matrix plagioclase has weak zoning (core:  $An_{27}$ ; rim:  $An_{24}$ ). Plagioclase inclusions within garnet range in anorthite content ( $An_{24-33}$ ) and are typically located in fractures. Matrix muscovite cores have lower Fe# (0.64–0.66) than rims (0.67–0.69). Abundant sillimanite fibres are present primarily within biotite.

Sample BU12-212B is a sillimanite–garnet metapelite collected in the structural middle of the upper-GH within massive marble and calc-silicates, 5.7 km and



12.4 km above the KT and MCT, respectively (Figs 2, 3e & 7). The metapelite was a thin (metre-scale) layer within calc-silicate. Biotite and sillimanite with minor muscovite combined with quartz ribbons define a strong schistose fabric in the metapelite (Fig. 5e). Garnet is subidioblastic, and many grains are elongate (up to 8 mm in length), adding to the strong foliation. Abundant quartz and ilmenite inclusions in garnet are oriented perpendicular to the foliation plane (Fig. 4e). The garnet has flat  $X_{Mn}$  profiles, but subtle zoning in  $X_{Mg}$ , with a homogenous core ( $X_{Mg} = 0.07$ ) that decreases slightly on the outermost rim ( $X_{Mg} = 0.06$ ) (Fig. 7). Grossular is typically highest in the core and outermost rim ( $X_{Ca} = 0.06$ ) and lowest,  $\sim 500$   $\mu m$  interior of the rim ( $X_{Ca} = 0.02$ ), whereas Fe# increases from core (0.92) to rim (0.94). Biotite in pressure shadows has Fe# of 0.78–0.81, whereas relatively lower Fe# (0.75–0.78) is observed in the matrix. Matrix biotite adjacent to garnet ranges in Ti (0.29–0.50 apfu) and is unzoned, whereas inclusions within garnet show an increase in Fe# (0.67–0.70) and Ti (0.32–0.38 apfu) from garnet core to rim. Most plagioclase is albitic ( $An_{01-06}$ ) and is very sparse within the sample. Where present, it is found within fractured K-feldspar ( $K/(K+Na+Ca) = 0.58$ ). This is the only sample that shows K-feldspar as the dominant feldspar. Muscovite in the matrix exhibits relatively consistent Fe# of 0.69–0.70, except when adjacent to biotite (0.79). Sillimanite occurs as thick fibrolitic mats along the foliation plane.

The structurally highest sample collected on the Kuru Chu transect (7 km and 14 km above the KT and MCT, respectively), BU12-221, is a sillimanite-bearing orthogneiss (Figs 2 & 7). This sample is part of a larger orthogneiss body that comprises the highest structural level that we were able to observe on this transect. Biotite and muscovite define a weak foliation (Fig. 5f), and a few of the muscovite grains exhibit symplectitic textures with K-feldspar. Garnet is idioblastic to subidioblastic, up to 2 mm in diameter, fractured and contains sparse quartz and plagioclase inclusions. Spessartine and Fe# are relatively homogeneous in the garnet core ( $X_{Mn} = 0.18$ ; Fe# = 0.88) and increase at the garnet rim ( $X_{Mn} = 0.25$ ; Fe# = 0.90) (Fig. 7). Grossular in garnet is relatively homogenous ( $X_{Ca} = 0.04$ –0.05). Matrix biotite has relatively homogenous Fe# of 0.67–0.69. Matrix biotite varies in Ti from 0.25 to 0.34 apfu and is unzoned, whereas in biotite located in garnet pressure shadows there is a relatively lower range (0.13–0.26 apfu). Matrix plagioclase is zoned, with low Ca cores ( $An_{19}$ ) in comparison to the rims ( $An_{23-25}$ ), whereas plagioclase in pressure shadows and adjacent to garnet has relatively lower anorthite ( $An_{18}$ ). Plagioclase inclusions in garnet cores are higher in Ca ( $An_{28-32}$ ). Muscovite in the matrix has higher Fe# cores ( $\sim 0.72$ ) and lower Fe# rims ( $\sim 0.69$ ). Sillimanite is present as clusters of fibrolite within muscovite.

## PRESSURE–TEMPERATURE RESULTS

### Bumthang Chu transect

From the Bumthang Chu transect, lower-GH kyanite–garnet metapelite (BU13-01B) records 660–680 °C using THERMOCALC, and Ti-in-biotite minimum estimates of 610–675 °C (Figs 8a & 9a). Structurally above this, two lower-GH metapelites (BU13-13A and BU13-18B) give similar temperatures of  $\sim 600$ –610 °C (THERMOCALC), and lower Ti-in-biotite temperature minimum estimates of 550–630 °C. Moreover, Ti-in-biotite minimum temperature estimates from metapelite BU13-13A suggest an increase during the transition to prograde-to-near-peak metamorphism, from  $\sim 470$  to  $\sim 600$  °C (Fig. 9a). Pressures from these three samples decrease moving structurally higher in the lower-GH, from  $8.9 \pm 1.3$  to  $6.5 \pm 0.9$  kbar just below the KT (Fig. 10a).

Structurally above the KT, peak temperatures of  $\sim 650$  °C (THERMOCALC) and  $\sim 600$ –650 °C (Ti-in-biotite) and a pressure of  $6.7 \pm 0.6$  kbar from metapelite BU13-23B are similar to lower-GH samples (Figs 8a & 9a). Metapelite BU13-43A is located  $\sim 200$  m structural distance above BU13-23B and reveals higher pressures ( $9.0 \pm 2.3$  kbar) and temperatures, including  $715 \pm 135$  °C (THERMOCALC) and 585–615 °C (Ti-in-biotite minimum *T*); however, only three reactions were formulated in THERMOCALC leading to poorly constrained *P*–*T* estimates with large errors and thus the results are within error of the lower-GH samples and BU13-23B (Fig. 8a; Table 2). The structurally highest Bumthang Chu sample (3.2 km structurally above the KT), orthogneiss BU13-42B, reveals a pressure of  $8.0 \pm 1.2$  kbar, and the temperature ranges from  $\sim 680$  to 690 °C (THERMOCALC) and 700 to 715 °C (Ti-in-biotite minimum temperature). Multiple samples from the upper-GH also record intra-sample Ti-in-biotite temperature differences between biotite inclusions in garnet and matrix biotite:  $\sim 600$  to  $\sim 650$  °C (BU13-23B) and  $\sim 550$  to  $\sim 610$  °C (BU13-43A) (Fig. 8a). These differences within these individual samples likely record the transition from prograde to near-peak metamorphism.

### Kuru Chu transect

From the Kuru Chu transect in northeastern Bhutan, two lower-GH kyanite–garnet metapelites (BU12-182 & BU12-187) record similar peak *P*–*T* conditions that are within error,  $9.0 \pm 1.1$  kbar and  $8.2 \pm 1.3$  kbar, respectively, with temperatures of  $\sim 660$ –720 °C (THERMOCALC) and  $\sim 630$ –675 °C (Ti-in-biotite minimum *T*) (Figs 8b & 9b). In comparison, a metapelite (BU12-198) that is within the KT zone records lower pressures ( $6.5 \pm 1.1$  kbar) and a narrow range of temperatures that are within error of the lower-GH samples, 670–685 °C (THERMOCALC) and 620–670 °C (Ti-in-biotite). Approximately 4 km

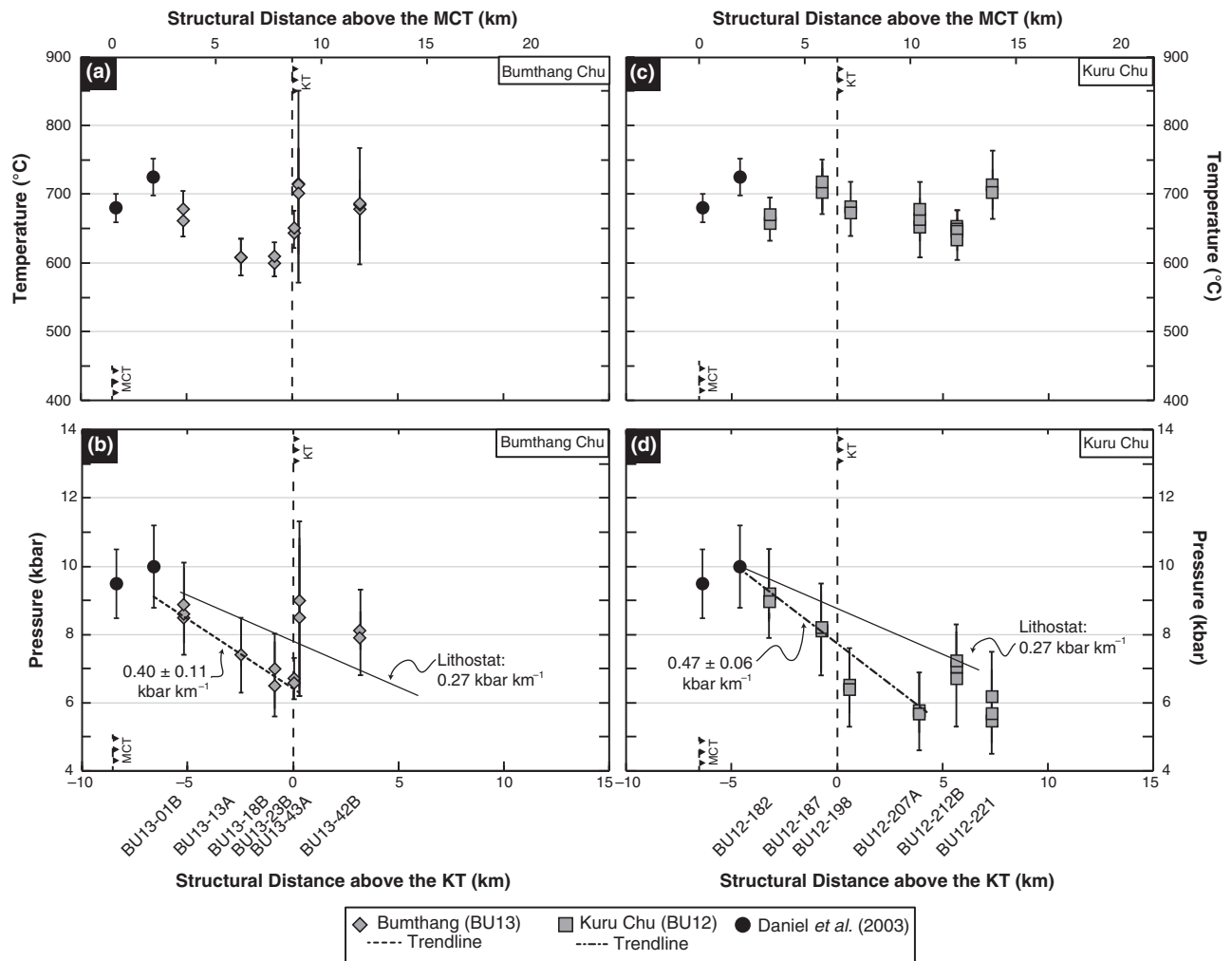


**Fig. 10.** Pressure–temperature–structural distance plots relative to the KT and the MCT for: (a and b) the Bumthang Chu transect, and (c and d) the Kuru Chu transect, with the temperature–structural distance diagrams shown in (a) and (c) and the pressure–structural distance diagrams in (b) and (d). In addition, for the pressure–structural distance diagrams, trend lines are shown for each transect, with the average lithostatic pressure for reference.  $P$ – $T$  data from Daniel *et al.* (2003) were also included for the determination of the trend lines. The regression lines were constructed using ISOPLOT (v.4.15; Ludwig, 2008). A conservative uncertainty ( $\pm 100$  m) was applied to the location of each sample within the structural column.

above the KT, metapelite BU12-207A reveals a pressure of  $5.7 \pm 1.1$  kbar that is within error of BU12-198, whereas temperatures are similar to the other samples,  $\sim 650$ – $680$  °C (THERMOCALC) and  $620$ – $670$  °C (Ti-in-biotite). Metapelite BU12-212B, located 5.7 km above the KT, yields temperature estimates of  $\sim 645 \pm 30$  °C (THERMOCALC) at  $\sim 7.0 \pm 1.1$  kbar (Fig. 8b). In comparison, the structurally highest sample from the Kuru Chu transect (BU12-221) records similar estimates of  $\sim 630$ – $650$  °C (THERMOCALC) and  $\sim 600$ – $660$  °C (Ti-in-biotite), and lower, but within error, estimates of  $5.7 \pm 1.0$  kbar (Figs 8b & 9b).

## DISCUSSION

Investigating how mid- to lower-crustal rocks are buried and subsequently exhumed in active

continental collisional orogenic systems can yield insight into the mechanisms by which an orogen evolves after collision. Textural, field and sample-scale relationships and  $P$ – $T$  conditions from GH samples collected along the two transects in central and eastern Bhutan are analysed below to better understand the burial history and evolution of the GH in the eastern Himalaya. These results are then compared to other studies of GH rocks exposed across the eastern Himalaya to compare differences and similarities in observed  $P$ – $T$  conditions along strike of the orogen.

### $P$ – $T$ results: evaluating the GH metamorphic history

Nearly all of the studied garnet exhibit relatively weak zoning in Ca, Fe, Mg and Mn, which is also observed in GH samples from other parts of the

central and eastern Himalaya (e.g. Daniel *et al.*, 2003; Jessup *et al.*, 2008; Kellett *et al.*, 2010; Warren *et al.*, 2014; Figs 6 & 7). The near-homogenous garnet compositional profiles for most samples suggest partial to complete diffusional reequilibration and modification of prograde zoning likely at high-temperature conditions (e.g. Yardley, 1977). In addition, as described above, the increase in  $X_{Mn}$  and Fe# at the garnet rims suggests retrograde effects (Spear, 1991; Kohn & Spear, 2000). Only one sample, BU13-18B, displays distinct garnet compositional profiles that decrease in  $X_{Ca}$ ,  $X_{Mn}$  and Fe# from core to rim, suggesting preservation of prograde garnet growth patterns (Fig. 6). Below we review the results from the individual transects, with the interpretation that the temperatures and pressures are likely near-peak thermal conditions when the garnet underwent reequilibration (e.g. Sorcar *et al.*, 2014). As many of the samples achieved pressures above the calibrated range for the Ti-in-biotite thermometer (4–6 kbar; Henry *et al.*, 2005), the THERMOCALC temperatures are interpreted to be the most representative of the reequilibration temperatures and are described below.

For the Bumthang Chu transect, all samples reveal temperatures within error of each other, ranging from ~700 to 600 °C (Fig. 10a). The pressures from these same samples record an overall decreasing trend within the lower-GH from ~10.0 to 6.5 kbar with increasing structural level above the MCT (Fig. 10b; including pressure data from Daniel *et al.* (2003), which was recalculated using THERMOCALC). Within this decreasing trend, moving from one sample to the next in structural position, the results are within error; however, comparing the sample at the structurally lowest position in the lower-GH v. within the KT zone, distinctly defines an upright pressure gradient of  $0.40 \pm 0.11$  kbar  $\text{km}^{-1}$ . This decreasing pressure trend is followed by an increase to ~8.0 kbar for the structurally highest sample exposed in the upper-GH (Fig. 10b; BU13-42B).

For the Kuru Chu transect, the temperature estimates from northeastern Bhutan are also within error, ranging from 630 to 730 °C (Fig. 10c). The pressure data for the structurally lower five samples, when including the recalculated pressure estimates of Daniel *et al.* (2003), show a similar overall upright trend to that in the Bumthang Chu, from ~10.0 to 5.7 kbar (pressure gradient of  $0.47 \pm 0.06$  kbar  $\text{km}^{-1}$ ).

Although there is evidence for diffusion and retrograde effects in the samples, when comparing both transects (Fig. 11), the samples show similar (upper) amphibolite facies conditions and trends in pressures and temperatures with increasing structural distance from the MCT. Moreover, some samples at similar structural distances from the MCT provide comparable pressure estimates. For example, kyanite–garnet metapelites, at 3.4 and 3.5 km structurally above the MCT (660–680 °C at 8.5–9.0 kbar), metapelites from

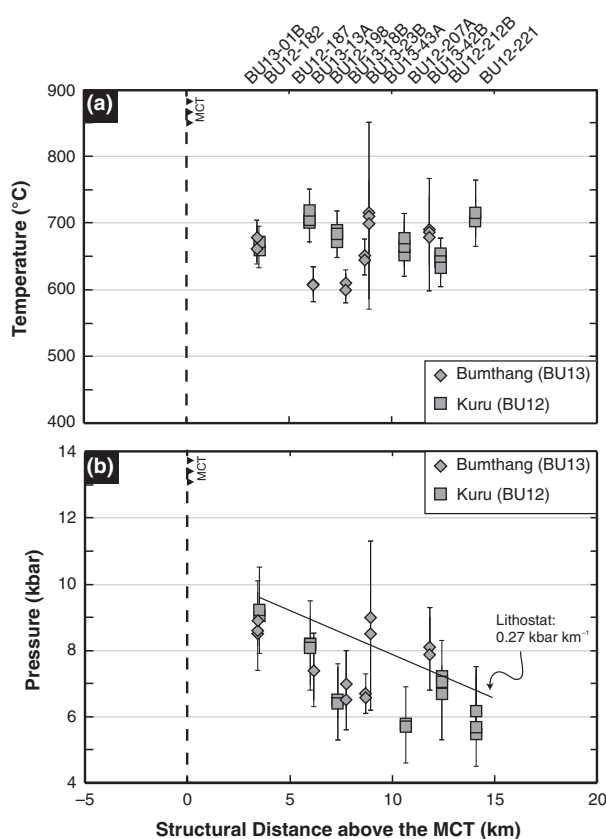


**Fig. 11.** (a) Temperature–structural distance and (b) pressure–structural distance plots relative to the MCT with the results from both transects plotted together. Average lithostatic pressure gradient is shown in (b) for reference.

6.0 to 6.2 km above the MCT (~7.4–8.2 kbar), and sillimanite–garnet metapelites from 7.3 to 7.7 km above the MCT (~6.5–7.0 kbar) reveal similar results.

In comparison, recent studies across the central and eastern Himalaya have revealed evidence that upper structural levels of the GH achieved granulite, and possibly earlier eclogite facies conditions prior to exhumation (e.g. Groppo *et al.*, 2010; Grujic *et al.*, 2011; Guilmette *et al.*, 2011; Warren *et al.*, 2011; Ambrose *et al.*, 2015; Zhang *et al.*, 2015). The upper-GH samples from central and eastern Bhutan in this study do not contain orthopyroxene or abundant K-feldspar and muscovite, observed in nearly all samples (the exception being BU12-212B), are interpreted to be part of the peak assemblage (Figs 4 & 5). Cordierite is also not found in GH samples from central and eastern Bhutan (Swapp & Hollister, 1991; this study). These results are very different than what has been documented for the equivalent upper-GH rocks in northwestern Bhutan. These notable petrological differences in the samples in both the peak (granulite facies assemblages) and the retrograde (cordierite-decompression textures) parts of the *P*–*T* path suggest fundamental differences in the tectonic history of the GH along strike across Bhutan.



### Construction of the GH

Overall, the new petrological data outline an upright apparent pressure gradient across the GH unit as a whole in central and eastern Bhutan (Figs 10 & 11). Zeiger *et al.* (2015) documented that the initiation of melt crystallization occurred earlier at structurally higher levels (~5 km above the KT), beginning at c. 27 Ma, with younger melt-crystallization ages (c. 16 Ma) closer to the MCT. Some of the analysed leucosomes were collected from the same outcrops as the samples studied here. These results were interpreted to reflect the construction of a composite GH unit by the progressive underplating of ductile material (Zeiger *et al.*, 2015). Under this interpretation, intra-GH shear zones may be present throughout the GH unit to accommodate this underplating. Within the overall upright pressure gradients observed in central and eastern Bhutan, the data suggest increases in pressure and in some cases, temperature (e.g. across the KT along the Bumthang Chu transect and at ~6 km above the KT along the Kuru Chu transect), although the *P–T* estimates are within error. These potential jumps in pressure  $\pm$  temperature may demarcate such shear zones.

Samples from both transects show minor ( $\leq 2$ –3 kbar,  $\leq 100$  °C, but within error) changes in *P–T* conditions near the previously mapped location of the KT, with an increase in pressure (although there are large errors on the data from sample BU13-43A) along the Bumthang Chu transect and an increase (but within error) in pressure ~5 km above the mapped KT along the Kuru Chu transect. The combined metamorphic and geochronometric data within GH rocks in central and eastern Bhutan suggest that the KT, as mapped, is potentially one of several shear zones, given the correlation of melt crystallization with structural level within the GH and the changes in pressure  $\pm$  temperature observed in the upper-GH along the transects that could have aided in the initial exhumation of ductile GH rocks (Fig. 12).

The rate at which the pressures decrease relative to structural level is greater than (1.5–1.7 times) a normal lithostatic gradient of  $\sim 0.27$  kbar km<sup>-1</sup>. The gradients revealed in central and eastern Bhutan may reflect a significant amount of post-metamorphic thinning of the composite GH unit, which would suggest that as underplating progressed, deeper, ductile GH rocks were emplaced, with the highest pressure conditions observed closer to the MCT. This is consistent with the super-lithostatic pressure gradients and layer-normal thinning documented through lower-GH rocks in south-central Bhutan (Long *et al.*, 2011c; Corrie *et al.*, 2012). Alternatively, the decreasing pressure gradient may reflect diachronous metamorphism resulting from the complex interplay of the shear zones (Fig. 12; e.g. Carosi *et al.*, 2010; Montomoli *et al.*, 2013). During initial motion on an individual shear zone, rocks in the hanging wall would begin their exhumation, whereas

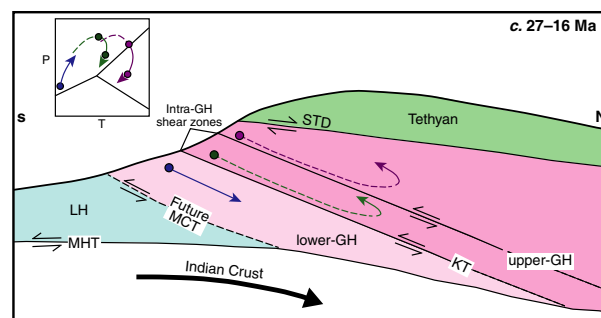


**Fig. 12.** Cartoon model of the progressive underplating of GH rocks along intra-GH shear zones. Representative rocks and the path they follow are shown by the coloured dots. These dots are also shown in the inset *P–T* diagram. The model highlights that increasing pressure with lower structural level within the GH is likely due to rocks in the footwall of a shear zone continuing to be buried as the hanging-wall rocks in the shear zone are being exhumed. Modified after Montomoli *et al.* (2013). GH, Greater Himalaya; LH, Lesser Himalaya; MCT, Main Central thrust; STD, Southern Tibetan detachment; KT, Kakhtang thrust.

rocks in the footwall would continue to be buried, reaching higher pressures compared to the rocks in the hanging wall. In comparison, temperatures across the transects are more consistent, likely due to thermal relaxation aided by heat advection via melt and magma migration (e.g. Imayama *et al.*, 2012; Wang *et al.*, 2013; Zeiger *et al.*, 2015); this thermal relaxation also likely caused the garnet reequilibration.

Evidence for intra-GH discontinuities and shear zones have been described from GH rocks across the Himalaya (Tibet to Nepal to Bhutan) based on a variety of data sets, including quartz lattice-preferred orientation data (e.g. Larson & Cottle, 2014) and single or combined petrological and geochronological data sets (e.g. Harris & Massey, 1994; Vannay & Hodges, 1996; Carosi *et al.*, 2010; Larson *et al.*, 2010; Yakymchuk & Godin, 2012; Montomoli *et al.*, 2013; Rubatto *et al.*, 2013; Wang *et al.*, 2013). Many of the petrological studies reveal a similar trend of decreasing pressure with increasing structural level within the composite GH unit. A decreasing pressure gradient is also predicted for rocks exhumed via a channel-flow model (e.g. Jamieson *et al.*, 2004), in which the GH represents a partially molten body of crustal material that is extruded to the south, driven by lateral pressure gradients and rapid erosion at the Himalayan topographic front (Beaumont *et al.*, 2001). However, throughout the lower-GH and parts of the upper-GH in Bhutan, there is not much evidence for a significant volume percentage of partial melt (e.g. Long & McQuarrie, 2010; this study). Moreover, a wedge-extrusion end-member model, where the GH is emplaced as a northward-tapering wedge (e.g. Hodges *et al.*, 1992; Grujic *et al.*, 1996; Vannay & Grasemann, 2001), as well as the channel-flow model (Beaumont *et al.*, 2001) predict similar

*P*–*T*–*t* behaviour across the composite GH unit, as both models require coeval activity of the lower and upper bounding structures (the MCT and STD, respectively). The trend in melt-crystallization ages from across the GH, and from many of the same outcrops studied here, argues for differential exhumation timing, with initial exhumation occurring first in the structurally highest rocks and later in structurally lower-GH rocks.

For central and eastern Bhutan, the new *P*–*T* results combined with the published melt-crystallization ages suggest progressive underplating of ductile GH rocks as the most likely emplacement mechanism for GH rocks in this part of the Himalaya (Fig. 12). Furthermore, given the melt-crystallization ages along these two transects (Zeiger *et al.*, 2015), activity along these intra-GH shear zones likely began at *c.* 27 Ma in the structurally highest levels, and continued to as late as *c.* 16 Ma in the structurally lower levels.

## CONCLUSIONS

New thermobarometry data from Greater Himalayan rocks in central and eastern Bhutan reveal that:

- 1 In central Bhutan, peak temperatures are within error in the lower- and upper-GH, ranging from  $\sim 730$  to  $600$  °C. Pressures decrease from 10.0 to 6.6 kbar in the lower-GH and within the KT zone before increasing to  $\sim 8.0$  kbar within the upper-GH. In eastern Bhutan, peak-temperature conditions range from 650 to 730 °C across the transect, and peak-pressure conditions generally decrease with increasing structural distance from the MCT from 10.0 kbar to 5.7 kbar structurally higher in the GH, with a minor jump in pressure at  $\sim 6$  km above the KT.
- 2 The decreasing pressure trends, the potential jumps in pressure observed in both transects and trends in melt-crystallization ages argue that the GH in central and eastern Bhutan was emplaced via progressive underplating of ductile material along at least one intra-GH shear zone, the KT, from likely *c.* 27 Ma in structurally higher levels of the GH to *c.* 16 Ma in structurally lower levels.
- 3 Super-lithostatic pressure gradients ( $0.40 \pm 0.11$  kbar  $\text{km}^{-1}$ , Bumthang Chu;  $0.47 \pm 0.06$  kbar  $\text{km}^{-1}$ , Kuru Chu) are documented in central and eastern Bhutan. These steep pressure gradients may represent significant layer-normal thinning during exhumation of the GH, or alternatively diachronous metamorphism related to shear zone activity before the composite GH unit was exhumed to shallow depths.

## ACKNOWLEDGEMENTS

Our research team thanks T. Tobgay, T. Tenzin, Sherub Wangdi and Wangchuk for their assistance

with logistics and fieldwork in Bhutan. We are also greatly indebted to U. Wangda, director of the Department of Geology and Mines in the Ministry of Economic Affairs. We thank C. Warren, K. Larson and an anonymous reviewer for their suggestions and insights into improvements on the early versions of this manuscript. C. Warren and C. Mottram are also thanked for their insightful conversations regarding the observations and geology in Sikkim, northwestern Bhutan and Arunachal Pradesh. T. Holland and C. Yakymchuk are also thanked for their correspondences regarding THERMOCALC *P*–*T* calculations. This project was made possible via funds from a National Science Foundation grant (EAR-1220300) awarded to S.P. Long and S.M. Gordon and partially funded via a Geological Society of America Graduate Student Research Grant awarded to K.S. Agustsson.

## REFERENCES

- Ambrose, T.K., Larson, K.P., Guilmette, C., Cottle, J.M., Buckingham, H. & Rai, S., 2015. Lateral extrusion, underplating, and out-of-sequence thrusting within the Himalayan metamorphic core, Kanchenjunga, Nepal. *Lithosphere*, **7**, 441–464.
- Armstrong, J.T., 1988. Quantitative analysis of silicates and oxide minerals: comparison of Monte-Carlo, ZAF and Phi-Rho-Z procedures. In *Microbeam Analysis* (ed. Newbury, D.E.), San Francisco Press, San Francisco, California, USA, pp. 239–246.
- Beaumont, C., Jamieson, R.A., Nguyen, M.H. & Lee, B., 2001. Himalayan tectonics explained by extrusion of a low-viscosity crustal channel coupled to focused surface denudation. *Nature*, **414**, 738–742.
- Bhargava, O.N., 1995. *The Bhutan Himalaya: A Geological Account*. Geological Survey of India, Kolkata, 245 pp.
- Brookfield, M.E., 1993. The Himalayan passive margin from Precambrian to Cretaceous times. *Sedimentary Geology*, **84**, 1–35. doi:10.1016/0037-0738(93)90042-4.
- Burchfiel, B.C., Chen, Z.L., Hodges, K.V. *et al.*, 1992. The South Tibetan detachment system, Himalayan Orogen: extension contemporaneous with and parallel to shortening in a collisional mountain belt. *Geological Society of America Special Paper*, **269**, 41.
- Carosi, R., Montomoli, C., Rubatto, D. & Visoná, D., 2010. Late Oligocene high-temperature shear zones in the core of the Higher Himalayan Crystallines (Lower Dolpo, western Nepal). *Tectonics*, **29**, 1–20. doi:10.1029/2008TC002400.
- Cooper, F.J., Hodges, K.V. & Adams, B.A., 2013. Metamorphic constraints on the character and displacement of the South Tibetan fault system, central Bhutanese Himalaya. *Lithosphere*, **5**, 67–81. doi:10.1130/L221.1.
- Corrie, S.L., Kohn, M.J., McQuarrie, N. & Long, S.P., 2012. Flattening the Bhutan Himalaya. *Earth and Planetary Science Letters*, **349–350**, 67–74.
- Daniel, C.G., Hollister, L.S., Parrish, R.R. & Grujic, D., 2003. Exhumation of the Main Central Thrust from Lower Crustal Depths, Eastern Bhutan Himalaya. *Journal of Metamorphic Geology*, **21**, 317–334.
- Davidson, C., Grujic, D.E., Hollister, L.S. & Schmid, S.M., 1997. Metamorphic reactions related to decompression and synkinematic intrusion of leucogranite, High Himalayan crystallines, Bhutan. *Journal of Metamorphic Geology*, **15**, 593–612.
- DeCelles, P.G., Gehrels, G.E., Quade, J., LaReau, B. & Spurlin, M., 2000. Tectonic implications of U–Pb zircon ages of the Himalayan Orogenic Belt in Nepal. *Science*, **288**, 497–499.

- Ding, L., Zhong, D., Yin, A., Kapp, P. & Harrison, T.M., 2001. Cenozoic structural and metamorphic evolution of the eastern Himalayan syntaxis (Namche Barwa). *Earth and Planetary Science Letters*, **192**, 423–438.
- Gaetani, M. & Garzanti, E., 1991. Multicyclic history of the northern India continental margin (northwestern Himalaya). *American Association of Petroleum Geologists Bulletin*, **75**, 1427–1446.
- Gansser, A., 1964. *The Geology of the Himalayas*. Wiley Interscience, New York, 289 pp.
- Gansser, A., 1983. *Geology of the Bhutan Himalaya*. Birkhauser Verlag, Basel, 181 pp.
- Garzanti, E., 1999. Stratigraphy and sedimentary history of the Nepal Tethys Himalaya passive margin. *Journal of Asian Earth Sciences*, **17**, 805–827. doi:10.1016/S1367-9120(99)00017-6.
- Greenwood, L.V., Argles, T.W., Parrish, R.R., Harris, N.B.W. & Warren, C., 2015. The geology and tectonics of central Bhutan. *Journal of the Geological Society*, **173**, 352–369. doi:10.1144/jgs2015-031.
- Groppo, C., Rubatto, D., Rolfo, F. & Lombardo, B., 2010. Early oligocene partial melting in the main central thrust zone (Arun valley, eastern Nepal Himalaya). *Lithos*, **118**, 287–301.
- Grujic, D., Casey, M., Davidson, C. *et al.*, 1996. Ductile extrusion of the Higher Himalayan Crystalline in Bhutan: evidence from quartz microfabrics. *Tectonophysics*, **260**, 21–43.
- Grujic, D., Hollister, L.S. & Parrish, R.R., 2002. Himalayan metamorphic sequence as an orogenic channel: insight from Bhutan. *Earth and Planetary Science Letters*, **198**, 177–191.
- Grujic, D., Warren, C.J. & Wooden, J.L., 2011. Rapid Synconvergent exhumation of Miocene-aged lower and orogenic crust in the eastern Himalaya. *Lithosphere*, **3**, 346–366.
- Guilmette, C., Indares, A. & Hebert, R., 2011. High-pressure anatexis paragneisses from the Namche Barwa, Eastern Himalayan Syntaxis: textural evidence for partial melting, phase equilibria modeling and tectonic implications. *Lithos*, **124**, 66–81.
- Harris, N. & Massey, J., 1994. Decompression and anatexis of Himalayan metapelites. *Tectonics*, **13**, 1537–1546.
- Harrison, T.M., Ryerson, F.J., LeFort, P., Yin, A., Lovera, O. & Catlos, E.J., 1997. A late Miocene-Pliocene origin for the central Himalayan inverted metamorphism. *Earth and Planetary Science Letters*, **146**, E1–E7. doi:10.1016/S0012-821X(96)00215-4.
- Heim, A. & Gansser, A., 1939. *Central Himalaya Geological Observations of Swiss Expedition*. Hindustan Publishing Corporation, India, pp. 1–246.
- Henry, D.J., Guidotti, C.V. & Thomson, J.A., 2005. The Ti-saturation surface for low-to-medium pressure metapelitic biotites: implications for geothermometry and Ti-substitution mechanisms. *American Mineralogist*, **90**, 316–328. doi:10.2138/am.2005.1498.
- Hodges, K.V., 2000. Tectonics of the Himalaya and southern Tibet from two perspectives. *Geologic Society of America Bulletin*, **112**, 324–350.
- Hodges, K.V., Parrish, R.R., Housh, T.B. *et al.*, 1992. Simultaneous Miocene extension and shortening in the Himalayan Orogen. *Science*, **258**, 1466–1470.
- Holdaway, M.J., 2000. Application of new experimental and garnet Margules data to the garnet-biotite geothermometer. *American Mineralogist*, **85**, 881–892.
- Holland, T.J.B. & Powell, R., 2003. Activity-composition relations for phases in petrological calculations: an asymmetric multicomponent formulation. *Contributions to Mineralogy and Petrology*, **145**, 492–501.
- Holland, T.J.B. & Powell, R., 2011. An improved and extended internally consistent thermodynamic dataset for phases of petrological interest, involving a new equation of state for solids. *Journal of Metamorphic Geology*, **29**, 333–383. doi:10.1111/j.1525-1314.2010.00923.x.
- Hollister, L.S. & Grujic, D., 2006. Pulsed channel flow in Bhutan. In: *Channel Flow, Extrusion, and Exhumation in Continental Collision Zones* (eds Law, R.D., Searle, M.P. & Godin, L.), *Geological Society London Special Publications*, **268**, 415–423.
- Imayama, T., Takeshita, T., Yi, K. *et al.*, 2012. Two-stage partial melting and contrasting cooling history within the Higher Himalayan Crystalline Sequence in the far-eastern Nepal Himalaya. *Lithos*, **134–135**, 1–22.
- Jamieson, R.A., Beaumont, C., Medvedev, S. & Nguyen, M.H., 2004. Crustal channel flows: 2. Numerical models with implications for metamorphism in the Himalayan-Tibet orogen. *Journal of Geophysical Research*, **109**, B06407.
- Jessup, M., Cottle, J., Searle, M. *et al.*, 2008. P-T-t-D paths of Everest Series schist. *Nepal. Journal of Metamorphic Geology*, **26**, 717–739.
- Kali, E., Leloup, P.H., Arnaud, N. *et al.*, 2010. Exhumation history of the deepest central Himalayan rocks, Ama Drime range: key pressure–temperature–deformation–time constraints on orogenic models. *Tectonics*, **29**, TC2014. http://dx.doi.org/10.1029/2009TC002551.
- Kellett, D.A., Grujic, D. & Erdmann, S., 2009. Miocene structural reorganization of the South Tibetan detachment, eastern Himalaya: Implications for continental collision: *Lithosphere*, **1**, 259–281. doi: 10.1130/L56.1.
- Kellett, D.A., Grujic, D., Warren, C., Cottle, J., Jamieson, R. & Tenzin, T., 2010. Metamorphic history of a syn-convergent orogen-parallel detachment: the South Tibetan detachment system, Bhutan Himalaya. *Journal of Metamorphic Geology*, **28**, 785–808.
- Kohn, M.J. & Spear, F., 2000. Retrograde net transfer reaction insurance for pressure-temperature estimates. *Geology*, **28**, 1127–1130.
- Kohn, M.J., Paul, S.K. & Corrie, S.L., 2010. The lower Lesser Himalayan Sequence: a Paleoproterozoic arc on the northern margin of the Indian plate. *Geological Society of America Bulletin*, **122**, 323–335. doi:10.1130/B26587.1.
- Larson, K.P. & Cottle, J.M., 2014. Midcrustal discontinuities and the assembly of the Himalayan midcrust. *Tectonics*, **33**, 718–740. doi:10.1002/2013TC003452.
- Larson, K.P., Godin, L. & Price, R.A., 2010. Relationships between displacement and distortion in orogens: linking the Himalayan foreland and hinterland in central Nepal. *Geological Society of America Bulletin*, **122**, 1116–1134. doi:10.1130/B30073.1.
- Leech, M.L., Singh, S., Jain, A.K., Klemperer, S.L. & Manickavasagam, R.M., 2005. The onset of India-Asia continental collision: early, steep subduction required by the timing of UHP metamorphism in the western Himalaya. *Earth and Planetary Science Letters*, **234**, 83–97.
- LeFort, P., 1975. Himalayas: the collided range. Present knowledge of the continental arc. *American Journal of Science*, **275-A**, 1–44.
- LeFort, P., Cuney, M., Deniel, C. *et al.*, 1987. Crustal generation of Himalayan leucogranites. *Tectonophysics*, **134**, 39–57.
- Long, S. & McQuarrie, N., 2010. Placing limits on channel flow: insights from the Bhutan Himalaya. *Earth and Planetary Science Letters*, **290**, 375–390.
- Long, S.P., McQuarrie, N., Tobgay, T., Grujic, D. & Hollister, L., 2011a. Geologic map of Bhutan. *The Journal of Maps*, **2011**, 184–192, 1:500,000-scale, doi: 10.4113/jom.2011.1159.
- Long, S., McQuarrie, N., Tobgay, T. & Grujic, D., 2011b. Geometry and crustal shortening of the Himalayan fold-thrust belt, eastern and central Bhutan. *Geologic Society of America Bulletin*, **123**, 1427–1447.
- Long, S., McQuarrie, N., Tobgay, T. & Hawthorne, J., 2011c. Quantifying internal strain and deformation temperature in the eastern Himalaya: implications for the evolution of strain in thrust sheets. *Journal of Structural Geology*, **32**, 579–608. doi:10.1016/j.jsg.2010.12.011.
- Long, S., McQuarrie, N., Tobgay, T., Rose, C., Gehrels, G. & Grujic, D., 2011d. Tectonostratigraphy of the Lesser



- Himalaya of Bhutan: implications for the along-strike stratigraphic continuity of the northern Indian margin. *Geological Society of America Bulletin*, **123**, 1406–1426. doi:10.1130/B30202.1.
- Ludwig, K.R., 2008. *Users Manual for Isoplot v.4.15/Ex: A Geochronological Toolkit for Microsoft Excel*. Berkeley Geochronology Center Special Publication, Berkeley, CA, 76 pp.
- Martin, A.J., Burg, K.D., Kaufman, A.J. & Gehrels, G.E., 2011. Stratigraphic and tectonic implications of field and isotopic constraints on depositional ages of Proterozoic Lesser Himalayan rocks in central Nepal. *Precambrian Research*, **185**, 1–17. doi:10.1016/j.precamres.2010.11.003.
- McLelland, J.M., Selleck, B.W., Bickford, M.E., 2010. Review of the Proterozoic evolution of the Grenville Province, its Adirondack outlier, and the Mesoproterozoic inliers of the Appalachians. In *From Rodinia to Pangea: The lithotectonic record of the Appalachian region* (eds Tollo, R.P., Bartholomew, M.J., Hibbard, J.P. & Karabinos, P.M.). *Geological Society of America Memoir*, **206**, 21–49. doi:10.1130/2010.1206(02).
- Montomoli, C., Iaccarino, S., Carosi, R., Langone, A. & Visonà, D., 2013. Tectonometamorphic discontinuities within the Greater Himalayan Sequence in Western Nepal (Central Himalaya): insights on the exhumation of crystalline rocks. *Tectonophysics*, **608**, 1349–1370.
- Myrow, P.M., Hughes, N.C., Searle, M.P., Fanning, C.M., Peng, S.C. & Parcha, S.K., 2009. Stratigraphic correlation of Cambrian–Ordovician deposits along the Himalaya: implications for the age and nature of rocks in the Mount Everest region. *Geological Society of America Bulletin*, **120**, 323–332.
- Penfold, M.L., Long, S.P., Gordon, S.M., Seward, G.G.E., Agustsson, K.S. & Zeiger, K.J., 2014. Deformation temperature, kinematics, and internal strain during emplacement of Greater Himalayan rocks in north-central and northeastern Bhutan: Abstract T21B-4596 presented at 2014 Fall Meeting, American Geophysical Union, San Francisco, California, 15–19 December.
- Powell, R. & Holland, T.J.B., 1988. An internally consistent thermodynamic dataset with uncertainties and correlations: 3: application methods, worked examples and a computer program. *Journal of Metamorphic Geology*, **6**, 173–204.
- Powell, R. & Holland, T.J.B., 1994. Optimal geothermometry and geobarometry. *American Mineralogist*, **79**, 120–133.
- Rowley, D.B., 1996. Age of initiation of collision between India and Asia: a review of stratigraphic data. *Earth and Planetary Science Letters*, **145**, 1–13.
- Rubatto, D., Chakraborty, S. & Dasgupta, S., 2013. Time-scales of crustal melting in the Higher Himalayan Crystallines (Sikkim, Eastern Himalaya) inferred from trace element-constrained monazite and zircon chronology. *Contributions to Mineralogy and Petrology*, **165**, 349–372.
- Searle, M., Simpson, R., Law, R., Parrish, R. & Waters, D., 2003. The structural geometry, metamorphic and magmatic evolution of the Everest massif, High Himalaya of Nepal–South Tibet. *Journal of the Geological Society*, **160**, 345–366.
- Sorcar, N., Hoppe, U., Dasgupta, S. & Chakraborty, S., 2014. High-temperature cooling histories of migmatites from the High Himalayan Crystallines in Sikkim, India: rapid cooling unrelated to exhumation? *Contributions to Mineralogy and Petrology*, **167**, 1–34.
- Spear, F.S., 1991. On the interpretation of peak metamorphic temperatures in light of garnet diffusion during cooling. *Journal of Metamorphic Geology*, **9**, 379–388.
- Suppe, J., 1983. Geometry and kinematics of fault-bend folding. *American Journal of Science*, **283**, 684–721.
- Swapp, S.M. & Hollister, L.S., 1991. Inverted metamorphism within the Tibetan slab of Bhutan: evidence for a tectonically transported heat-source. *Canadian Mineralogist*, **29**, 1019–1041.
- Vannay, J.C. & Grasemann, B., 2001. Himalayan inverted metamorphism and synconvergence extension as a consequence of a general shear extrusion. *Geological Magazine*, **138**, 253–276.
- Vannay, J.C. & Hodges, K.V., 1996. Tectonometamorphic evolution of the Himalayan metamorphic core between the Annapurna and Dhaulagiri, Central Nepal. *Journal of Metamorphic Geology*, **14**, 635–656.
- Wang, J.M., Zhang, J.J. & Wang, X.X., 2013. Structural kinematics, metamorphic P–T profiles and zircon geochronology across the Greater Himalayan Crystalline Complex in south-central Tibet: implication for a revised channel flow. *Journal of Metamorphic Geology*, **31**, 607–628.
- Warren, C.J., Grujic, D., Kellett, D.A., Cottle, J., Jamieson, R.A. & Ghalley, K.S., 2011. Probing the depths of the India–Asia collision: U–Th–Pb monazite chronology of granulites from NW Bhutan. *Tectonics*, **30**, TC2004.
- Warren, C.J., Grujic, D., Cottle, J.M. & Rogers, N.W., 2012. Constraining cooling histories: rutile and titanite chronology and diffusion modelling in NW Bhutan. *Journal of Metamorphic Geology*, **30**, 113–130. doi:10.1111/j.1525-1314.2011.00958.x.
- Warren, C., Singh, A.K., Roberts, N.M.W., Regis, D., Halton, A.M. & Singh, R.B., 2014. Timing and conditions of peak metamorphism and cooling across the Zimithang Thrust, Arunachal Pradesh, India. *Lithos*, **200–201**, 94–110. doi:10.1016/j.lithos.432.2014.04.005.
- Whitney, D.L. & Evans, B.W., 2010. Abbreviations for names of rock-forming minerals. *American Mineralogist*, **95**, 185–187.
- Yakymchuk, C. & Godin, L., 2012. Coupled role of deformation and metamorphism in the construction of inverted metamorphic sequences: an example from far-northwest Nepal. *Journal of Metamorphic Geology*, **30**, 513–535. doi:10.1111/j.1525-1314.2012.00979.x.
- Yardley, B.W.D., 1977. An empirical study of diffusion in garnet. *American Mineralogist*, **62**, 793–800.
- Yin, A., 2006. Cenozoic tectonic evolution of the Himalayan orogen as constrained by along-strike variation of structural geometry, exhumation history, and foreland sedimentation. *Earth Science Reviews*, **76**, 1–131. doi:10.1016/j.earscirev.2005.05.004.
- Yin, A. & Harrison, T.M., 2000. Geologic Evolution of the Himalayan–Tibetan Orogen. *Annual Review of Earth and Planetary Science*, **28**, 211–280.
- Zeiger, K., Gordon, S.M., Long, S.P., Kylander-Clark, A.R.C., Agustsson, K. & Penfold, M., 2015. Timing and conditions of metamorphism and melt crystallization in Greater Himalayan rocks, eastern and central Bhutan: insight from U–Pb zircon and monazite geochronology and trace-element analyses. *Contributions to Mineralogy and Petrology*, **169**, doi:10.1007/s00410-015-1143-6.
- Zhang, Z.M., Zhao, G.C., Wang, J.L., Dong, X. & Liou, J.G., 2010. Two stages of granulite facies metamorphism in the eastern Himalayan syntaxis, south Tibet: petrology, zircon geochronology and implications for the subduction of Neo-Tethys and the Indian continent beneath Asia. *Journal of Metamorphic Geology*, **28**, 719–733.
- Zhang, Z.M., Xiang, H., Dong, X. *et al.*, 2015. Oligocene HP metamorphism and anatexis of the Higher Himalayan Crystalline Sequence in Yadong region, east-central Himalaya. *Gondwana Research*, in press. doi:10.1016/j.gr.2015.03.002.

## SUPPORTING INFORMATION

Additional Supporting Information may be found in the online version of this article at the publisher's web site:

**Figure S1.** Cross-sections of the Kuru Chu and Bumthang Chu transects. The apparent dip of tectonic foliation at each measured outcrop is projected

onto the cross-section. Adjacent dip domains, defined by areas of common apparent dip, are separated by kink axes that bisect the interlimb angle (e.g. Suppe, 1983). Structural thickness (foliation-normal distance) above and below the MCT and KT was estimated from the cross-sections. Sub-surface geometry of Lesser Himalayan rocks on the Kuru Chu cross-section is taken from Long *et al.* (2011b). See Fig. 2 for guide to map units.

**Table S1.** Mineralogy used to calculate pressure–temperature estimates.

**Table S2.** Representative electron microprobe compositional analyses.

**Table S3.** Titanium-in-biotite temperature estimates.

*Received 26 October 2015; revision accepted 27 April 2016.*